

AD-A050 785

RCA LABS PRINCETON N J
RADIATION EFFECTS ON THE ELECTRICAL PROPERTIES OF MOS DEVICE MA--ETC(U)
FEB 78 G W HUGHES

DAAG39-76-C-0088

F/G 20/12

NL

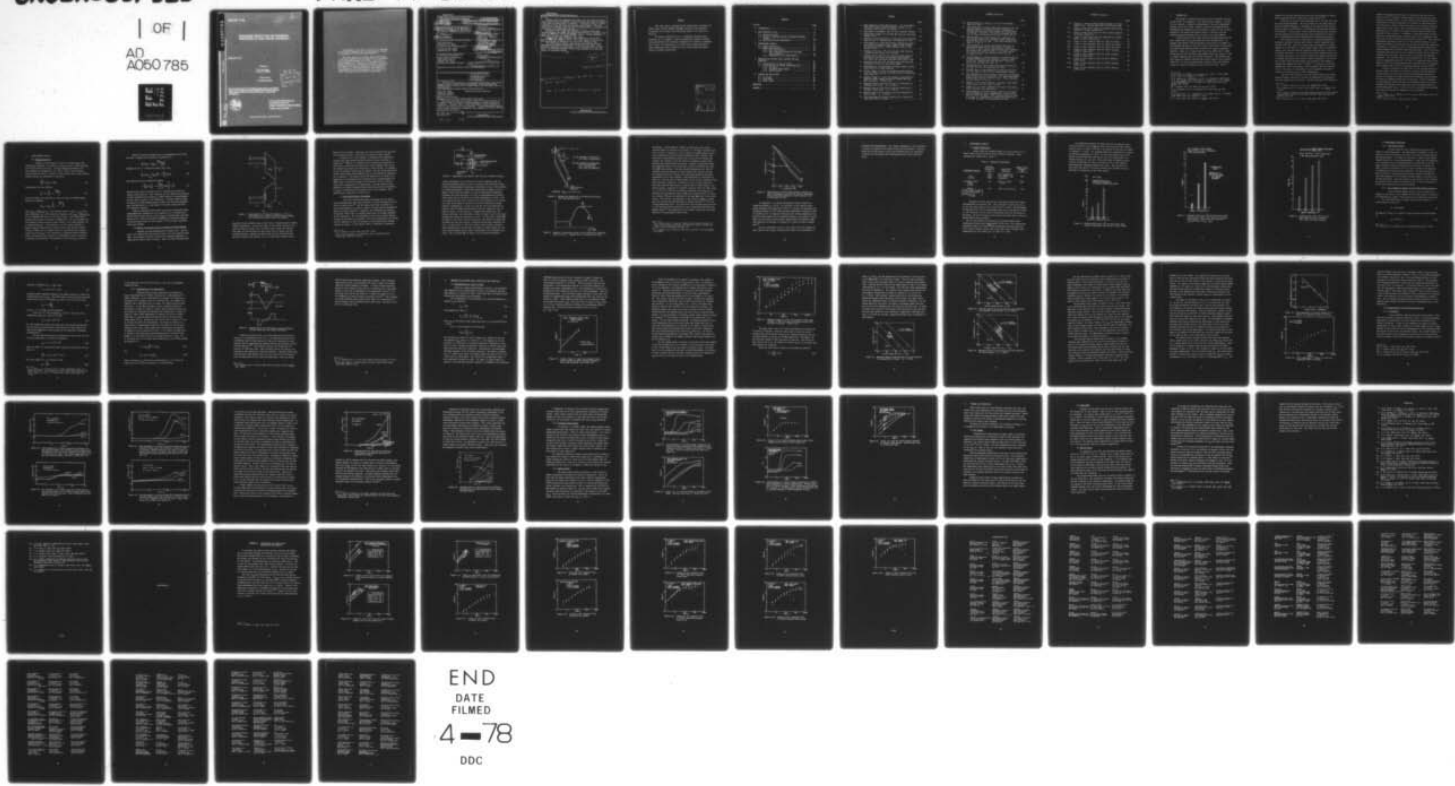
UNCLASSIFIED

PRRL-77-CR-37

HDL-CR-77-088

| OF |
AD
A050 785

FILE



END
DATE
FILED
4-78
DDC

AD A050285

HDL-CR-77-088

**RADIATION EFFECTS ON THE ELECTRICAL
PROPERTIES OF MOS DEVICE MATERIALS**

FEBRUARY 1978

HDL-CR-77-088, Radiation Effects on the Electrical Properties of MOS Device Materials.

By Gary W. Hughes

Prepared by

RCA Laboratories
Princeton, NJ 08540

Under Contract
DAAG39-76-C-0088

D D C
Declassified
MAR 6 1978
Releasable
A

This work was sponsored by the Defense Nuclear Agency under Nuclear Weapons Effects Research Subtask Z99QAXTA007 (Transient Radiation Effects Physics), Work Unit 61 (Surface Effects and Interface State Investigations).



**U.S. Army Materiel Development
and Readiness Command
HARRY DIAMOND LABORATORIES
Adelphi, Maryland 20783**

APPROVED FOR PUBLIC RELEASE; DISTRIBUTION UNLIMITED

DDC FILE COPY

The finding of this report are not to be construed as an official Department of the Army position, unless so designated by other authorized documents.

When this report is no longer needed, Department of the Army organizations will destroy it in accordance with the procedure given in AR 380-5. Navy and Air Force elements will destroy it in accordance with applicable directives. Department of Defense contractors will destroy the report according to the requirements of section 14 of the Industrial Security Manual for Safeguarding Classified Information. All others will return the report to Harry Diamond Laboratories.

UNCLASSIFIED

SECURITY CLASSIFICATION OF THIS PAGE (When Data Entered)

19 REPORT DOCUMENTATION PAGE		READ INSTRUCTIONS BEFORE COMPLETING FORM
1. REPORT NUMBER 18 HDL-CR-77-088	2. GOVT ACCESSION NO. 9 Final rept.	3. RECIPIENT'S CATALOG NUMBER 2 Mar 76-28 Feb 77,
4. TITLE (and Subtitle) 6 RADIATION EFFECTS ON THE ELECTRICAL PROPERTIES OF MOS DEVICE MATERIALS.	5. TYPE OF REPORT & PERIOD COVERED Final Report (3-2-76 to 2-28-77)	
7. AUTHOR(s) 10 Gary W. Hughes	6. PERFORMING ORG. REPORT NUMBER 11 PRRL-77-CR-37	
9. PERFORMING ORGANIZATION NAME AND ADDRESS RCA Laboratories Princeton, NJ 08540	8. CONTRACT OR GRANT NUMBER(s) DAAG39-76-C-0088 <i>new</i> DRCMS Code: 697000.22 MIPR 76-654	
11. CONTROLLING OFFICE NAME AND ADDRESS Defense Nuclear Agency Washington, DC 20305	10. PROGRAM ELEMENT, PROJECT, TASK AREA & WORK UNIT NUMBERS Prog Element: 6.27.04 Subtask: Z99QAXTA007 HDL Project: 236628	
12. REPORT DATE 11 February 1978	13. NUMBER OF PAGES 71 (12) 63 P.	
14. MONITORING AGENCY NAME & ADDRESS (if different from Controlling Office) Harry Diamond Laboratories 2800 Powder Mill Rd Adelphi, MD 20783	15. SECURITY CLASS. (of this report) Unclassified	
16. DISTRIBUTION STATEMENT (of this Report) Approved for public release; distribution unlimited.	15 DAAG39-76-C-0088, DNA-MIPR-76-654	
17. DISTRIBUTION STATEMENT (of the abstract entered in Block 20, if different from Report) 16 Z99QAXT 17 A007		
18. SUPPLEMENTARY NOTES This work was sponsored by the Defense Nuclear Agency under Nuclear Weapons Effects Research Subtask Z99QAXTA007 (Transient Radiation Effects Physics), Work Unit 61 (Surface Effects and Interface State Investigations).		
19. KEY WORDS (Continue on reverse side if necessary and identify by block number) SiO ₂ , MOS, CMOS Radiation Hardness Interface States Capture Cross Sections	Vacuum Ultraviolet Radiation	
20. ABSTRACT (Continue on reverse side if necessary and identify by block number) Radiation-hard SiO ₂ on Si grown by three different processes (dry, pyrogenic steam, and hybrid) has been examined by vacuum ultraviolet techniques. Flatband shift vs time measurements provide estimates of capture cross sections and trap densities. Current-enhancement measurements provide qualitative information about trapping at both the Si-SiO ₂ and gate-SiO ₂ interface.		

DD FORM 1473
1 JAN 73

UNCLASSIFIED

SECURITY CLASSIFICATION OF THIS PAGE (When Data Entered)

299 000

50B

UNCLASSIFIED

SECURITY CLASSIFICATION OF THIS PAGE (When Data Entered)

20.

Results show that unannealed dry oxides have the lowest interface-state density after irradiation, making them more desirable for applications where switching speed is important. Annealing in argon at 800°C increases both the hole-trap and interface-state density. All dry oxides have a dominant trap with capture cross section $S \propto 5 \times 10^{-14} \text{ cm}^2$ at applied oxide fields $E_0 = 1 \text{ MV/cm}$. E_0 sub 0

Pyrogenic steam oxides have many more interface states after irradiation than dry oxides and can be characterized by a dominant trap with $S \propto 5 \times 10^{-14} - 10^{-13} \text{ cm}^2$ for $E_0 = 1 \text{ MV/cm}$. Oxides annealed at 900°C have the smallest density of hole traps.

Hybrid oxides grown in 3% HCl steam followed by dry O₂ show $S \propto 2 \times 10^{-13} \text{ cm}^2$ at $E_0 = 1 \text{ MV/cm}$. The larger capture cross section for these oxides is believed to be due to the presence of HCl.

All oxides show a neutral trap capture cross section which is approximately inversely proportional to applied oxide field. Both pyrogenic steam and dry hard oxides can be characterized by the same trap. The difference between the two oxides appears to be only the density of interface states.

approx. \propto

5×10 to the -14^{th} power sq. cm.

* 5×10 to the -14^{th} power to 10 to the -13^{th} power sq. cm.

** 2×10 to the -13^{th} power sq. cm.

UNCLASSIFIED

SECURITY CLASSIFICATION OF THIS PAGE (When Data Entered)

PREFACE

This final report, prepared by RCA Laboratories, Princeton, NJ 08540, under Contract DAAG39-76-C-0088, describes work performed principally in the Solid State Technology Center, J. H. Scott, Jr., Director.

The Project Supervisor is K. H. Zaininger, and the Project Scientist is G. W. Hughes. Device processing and radiation testing were performed with the competent assistance of M. Morad, R. Snedeker, and F. Taft. The assistance of J. Fabula and S. Cohen, RCA Solid State Technology Center, Somerville, NJ, in fabricating the hybrid oxides is greatly appreciated.

ACCESSION NO.	
NTIS	White Section <input checked="" type="checkbox"/>
PPS	Ref. Section <input type="checkbox"/>
UNARMED	
JUSTIFICATION	
BY	
DISTRIBUTION/AVAILABILITY CODE	
DIGI.	AVAIL. REG/IR SPECIAL
A	

CONTENTS

Section	Page
1. INTRODUCTION	8
2. HOLE TRAPPING IN SiO ₂	11
2.1 Trapping Kinetics	11
2.2 Effect of Interface States on Measured Flatband Voltage	12
2.3 High Field-Current Enhancement	14
3. EXPERIMENTAL METHODS	20
3.1 Sample Preparation	20
3.2 Measurement Techniques	24
3.2.1 Hole Photocurrents	24
3.2.2 Dose Comparison Between VUV and High Energy Radiation	24
3.2.3 Deep-Depletion C-V Measurements	26
4. MEASURED HOLE CAPTURE CROSS SECTIONS AND TRAP DENSITIES	29
4.1 Interpretation of ΔV_{FB} vs t Data	29
4.2 Interpretation of Current Enhancement Data	38
4.2.1 Dry Oxides	38
4.2.2 Pyrogenic Steam Oxides	44
4.2.3 Hybrid Oxides	44
5. SUMMARY AND CONCLUSIONS	48
5.1 Dry Oxides	48
5.2 Steam Oxide	49
5.3 Hybrid Oxides	49
REFERENCES	52
APPENDIX	55

FIGURES

	<i>Page</i>
1. Band diagram of Si-SiO ₂ MOS capacitor. (a) In accumulation, only acceptor interface-states charged; (b) in inversion, mostly donors are charged	13
2. Experimental arrangement used for hole transport studies	15
3. Energy band diagram of an Si-SiO ₂ MOS structure with high applied field	16
4. Behavior of measured current vs time under bias conditions shown in fig. 3. Numbers refer to discussion in text	16
5. Band diagram of Si-SiO ₂ MOS interface showing the effect of positive and negative sheet charge on band bending and tunneling distance. Roman numerals refer to discussion in text	18
6. Flatband shift after 10 ⁶ rad total dose 1-MeV electron irradiation (10 ⁴ rad/s) for dry oxides	21
7. Flatband shift after 10 ⁶ rad total dose 1-MeV electron irradiation (10 ⁴ rad/s) for pyrogenic steam oxides. Both actual and normalized $ \Delta V_{FB} $ data shown ($\Delta V_{FG} \propto d_{ox}^2$)	22
8. Flatband shift after 10 ⁶ rad total dose 1-MeV electron irradiation (10 ⁴ rad/s) for hybrid oxides	23
9. Deep-depletion C-V measurement technique showing circuit connections and voltage waveforms	27
10. Initial $ \Delta V_{FB} $ vs t data for pyrogenic steam oxide annealed at 900°C, showing relaxation effect and resulting unity slope line	30
11. Complete $ \Delta V_{FB} $ vs t data for pyrogenic steam oxide annealed at 900°C showing differences between DDCV and HFCV techniques. 5-MV/cm bias	32
12. Measured capture cross sections and trap densities for unannealed dry oxides. $E_0 = 1$ MV/cm	33
13. Measured capture cross section and trap densities for pyrogenic steam oxides. $E_0 = 1$ MV/cm	34
14. Measured capture cross sections and trap densities for hybrid oxides. $E_0 = 1$ MV/cm	34
15. Field dependence of initial probability of capture for unannealed 1000°C dry oxide	37

FIGURES (Continued)

	Page
16. Field dependence of $ \Delta V_{FB} $ vs t data for unannealed 1000°C dry oxide	37
17. Time dependence of current during VUV irradiation for dry O ₂ -grown samples with different growth temperatures. Positive gate bias was used to produce an average field of 6 MV/cm in the oxide. The photon energy was 10.2 eV and the SiO ₂ absorbed photon flux was $4 \times 10^{11} \text{ cm}^{-2} \text{ s}^{-1}$	39
18. Time dependence of current during VUV irradiation for dry O ₂ -grown samples with different growth temperatures. Negative gate bias was used. Other conditions were the same as in fig. 17	39
19. Time dependence of current during VUV irradiation for dry O ₂ -grown samples which were annealed in argon at 800°C for 15 min. Positive gate bias was used to produce an average oxide field of 6 MV/cm. The photon energy was 10.2 eV and the SiO ₂ absorbed photon flux was $4 \times 10^{11} \text{ cm}^{-2} \text{ s}^{-1}$	40
20. Time dependence of current during VUV irradiation for dry O ₂ -grown samples which were annealed in argon at 800°C for 15 min. Negative gate bias was used. Other conditions are the same as in fig. 19	40
21. Flatband shift vs time during irradiation with positive and negative bias for unannealed dry oxides	42
22. Flatband shift vs time during VUV irradiation with positive and negative gate bias for argon-annealed oxides	43
23. Time dependence of current during irradiation for pyrogenic steam oxides which were annealed at the temperatures shown. Positive gate bias of 5 MV/cm was used. Other conditions were the same as in fig. 17	45
24. $ \Delta V_{FB} $ vs t for various anneals of pyrogenic steam oxide. Positive gate bias of 5 MV/cm was used	45
25. $ \Delta V_{FB} $ vs t for 1150°C annealed hybrid oxide illustrating little interface state generation	46
26. Time dependence of current during irradiation for hybrid oxides annealed at various temperatures. Positive gate bias of 5 MV/cm was used. Other conditions were the same as in fig. 17. Differences in initial photocurrent due to varying thickness of semitransparent Al gate	46

FIGURES (Continued)

	Page
27. $ \Delta V_{FB} $ vs t data for hybrid oxides annealed at various temperatures. Positive gate bias of 5 MV/cm was used .	47
A-1. $ \Delta V_{FB} $ vs time "early" data for pyrogenic steam oxides annealed at various temperatures	56
A-2. $ \Delta V_{FB} $ vs time "early" data for hybrid oxides annealed at various temperatures	56
A-3. $ \Delta V_{FB} $ vs time "early" data for unannealed dry oxides grown at various temperatures	57
A-4. $ \Delta V_{FB} $ vs time "complete" data for 900°C dry oxides . .	57
A-5. $ \Delta V_{FB} $ vs time "complete" data for 1000°C dry oxides . .	58
A-6. $ \Delta V_{FB} $ vs time "complete" data for 1150°C dry oxides . .	58
A-7. $ \Delta V_{FB} $ vs time "complete" data for 1000°C annealed pyrogenic steam oxide	59
A-8. $ \Delta V_{FB} $ vs time "complete" data for 1100°C annealed pyrogenic steam oxide	59
A-9. $ \Delta V_{FB} $ vs time "complete" data for 925°C annealed hybrid oxide	60
A-10. $ \Delta V_{FB} $ vs time "complete" data for 1000°C annealed hybrid oxide	60
A-11. $ \Delta V_{FB} $ vs time "complete" data for 1075°C annealed hybrid oxide	61

1. INTRODUCTION

The growth of radiation-hard SiO_2 for MOS integrated circuits is now within the capability of the semiconductor industry. In spite of this, however, a complete understanding of the basic degradation problem is not yet in hand. Recently work has been reported which illuminates the mechanism of hole transport in SiO_2 ,¹⁻³ but an understanding of the atomic and chemical nature of the hole trap and radiation-induced interface state in SiO_2 is far from complete.

Several models of hole traps have been proposed based upon the short range order of SiO_2 and band structure considerations. Di-Stephano and Eastman⁴ used photoemission spectroscopy to examine the valence-band structure of SiO_2 and found a narrow band of states near the valence-band edge which they attributed to oxygen non-bonding orbitals. Sigel et al. showed that SiO_2 films exhibit an E' center during electron spin resonance measurements which they believe is due to oxygen vacancies near the Si- SiO_2 interface.⁵ Sah believes that hole traps are primarily interstitial oxygen vacancies and trivalent silicons.⁶ It is also possible that some hole traps and interface states are caused by impurity species within the SiO_2 . This is

¹J. R. Srour, S. Othmer, O. L. Curtis, Jr., and K. Y. Chiu, *IEEE Trans. Nucl. Sci.* NS-23, 1513 (1976).

²F. B. McLean, H. E. Boesch, Jr., and J. M. McGarrity, *IEEE Trans. Nucl. Sci.* NS-23, 1506 (1976) and H. E. Boesch, Jr., F. B. McLean, J. M. McGarrity, and G. A. Ausman, Jr., *IEEE Trans. Nucl. Sci.* NS-22, 2163 (1975).

³R. C. Hughes, *Bull. Am. Phys. Soc.* 21, 404 (1976).

⁴T. H. DiStephano and D. E. Eastman, *Sol. State Comm.* 9, 2259 (1971).

⁵G. H. Sigel, Jr., E. J. Friebele, R. J. Ginther, and D. L. Griscom, *IEEE Trans. Nucl. Sci.* NS-21, 56 (1974).

⁶C. T. Sah, *IEEE Trans. Nucl. Sci.* NS-23, 1563 (1976).

supported by the many observations that show the difficulty of fabricating consistently hard oxides with a given process.^{7,8}

Whatever the nature of hole traps may be, it is clear that they are very process-dependent. For those traps that are deep enough to prevent thermal detrapping, a knowledge of the capture cross section and trap density is sufficient to characterize the radiation response of the oxide. In this report we have measured capture cross sections and trap densities for many different process variations in order to try to understand the process dependence of radiation-hard oxides.

The characterization of hard oxides is usually determined by a flatband or threshold voltage shift after a certain radiation dose, typically 10^6 rad. While the voltage shift thus measured is usually assumed to be due mainly to oxide trapped charge, there is evidence to suggest that radiation-induced interface states may play a role that is equally important. It is possible that these interface states may be largely responsible for the wide variation in radiation sensitivity of thermal SiO_2 grown under similar process conditions.⁹ Our recent work in fact shows that hard oxides can be grown in dry oxygen at temperatures ranging from 900° to 1050°C .⁹ In the past it has been assumed that 1000°C was optimum. This conclusion may have resulted from an occurrence of large numbers of post-irradiation interface states in the oxides grown at other temperatures.

The role that interface states and oxide traps play in determining radiation sensitivity can only be determined by a technique that can separate the two effects. Recently Ning and Yu¹⁰ reported a

⁷B. L. Gregory, *IEEE Trans. Nucl. Sci.* NS-22, 2295 (1975).

⁸G. W. Hughes and R. J. Powell, *IEEE Trans. Nucl. Sci.* NS-23, 1569 (1976).

⁹G. W. Hughes, "Radiation and Charge Transport in SiO_2 ," Final Report prepared under Contract N00014-74-C-0185 for Office of Naval Research, July 1977.

¹⁰T. H. Ning and H. N. Yu, *J. Appl. Phys.* 45, 5373 (1974).

method for studying electron traps in SiO_2 which has been used by Aitken et al.¹¹ to measure electron capture cross sections and trap densities of thermal SiO_2 . In this technique, the measured flatband voltage shift of an MOS capacitor as a function of time during electron injection is used to derive the capture cross section S and trap density N_T of oxide traps. This technique was also developed independently by R. J. Powell for capture of holes during the first two quarters of this contract. In addition to this method Powell has developed a current-enhancement technique which gives information about hole traps at both the Si-SiO_2 and gate- SiO_2 interface.¹² This current-enhancement phenomenon proves to be a very sensitive measure of the number and location of traps near the Si-SiO_2 and gate- SiO_2 interfaces. Furthermore, it provides a tool for comparing radiation sensitivity between samples with different processing histories. Both of the above techniques have been used here in a slightly modified form to draw conclusions about the nature of hole traps in SiO_2 grown by different processes. The processes that we have examined are: (1) dry oxides grown at temperatures from 900° to 1150°C ; (2) pyrogenic steam oxides grown at 875°C and annealed between 900° and 1100°C ; and (3) pyrogenic hybrid oxides grown at 925°C and annealed between 925° and 1150°C .

Section 2 discusses the model used for the trapping kinetics of holes in SiO_2 , the effects of interface states on measured flatband voltage shifts, and the high field current-enhancement phenomenon. Section 3 discusses the sample preparation techniques and the methods by which the trapping parameters were measured. Section 4 presents the experimental results and makes interpretations about the nature of trapping and interface-state generation from the flatband shift and current-enhancement data. Finally, Section 5 summarizes and concludes with some observations and suggestions for future work.

¹¹J. M. Aitken, D. J. DiMaria, and D. R. Young, *IEEE Trans. Nucl. Sci.* NS-23, 1526 (1976).

¹²R. J. Powell, *J. Appl. Phys.* 46, 4557 (1975).

2. HOLE TRAPPING IN SiO_2

2.1 Trapping Kinetics

Consider a distribution of traps in a narrow region near the Si-SiO_2 interface. Let there be N_T traps per cm^2 of which N_T^+ traps per cm^2 are filled with holes. Then the trapping probability of a hole reaching the interface is $(N_T - N_T^+) S$, where S is the capture cross section for holes. Letting J be the constant hole current density flowing through the interface, we can write:

$$\frac{dN_T^+}{dt} = \frac{J}{q} (N_T - N_T^+) S \quad (1)$$

This equation has the solution:

$$N_T^+ = N_T \left(1 - e^{-\frac{JSt}{q}} \right) \quad (2)$$

and if we express the densities of traps in terms of flatband shift, equation (2) becomes:

$$\Delta V_{FB} = \Delta V_{FBF} \left(1 - e^{-\frac{JSt}{q}} \right) \quad (3)$$

where $\Delta V_{FB} = (qN_T^+ d_{ox})/\epsilon_{ox}$ is the flatband shift at time t , d_{ox} is the oxide thickness, ϵ_{ox} is the dielectric constant, and $\Delta V_{FBF} = (qN_T d_{ox})/\epsilon_{ox}$ is the flatband shift with all the traps filled. This simple model assumes that emission from traps is unimportant. One can determine the trap density N_T and the capture cross section S by fitting equation (3) to experimental data. Unfortunately, it is not always possible to measure ΔV_{FBF} directly because tunnel injection may prevent complete filling of traps, and the highest value of ΔV_{FB} reached may be appreciably less than ΔV_{FBF} . More importantly, radiation-induced interface states at saturation can account for a substantial amount of positive or negative charge making a determination of N_T from ΔV_{FBF} difficult.

There are several alternate ways of determining N_T and S from the data. Consider the derivative of equation (3):

$$\frac{d}{dt} \Delta V_{FB} = \Delta V_{FBF} e^{-\frac{JS}{q}} \left(\frac{JS}{q} \right) \quad (4)$$

Equation (4) at $t = 0$ gives the product $N_T S$, e.g.,

$$\left| \frac{d}{dt} \Delta V_{FB} \right|_{t=0} = \Delta V_{FBF} \frac{JS}{q} = J \frac{d_{ox}}{\epsilon_{ox}} (N_T S) \quad (5)$$

Also taking the log of equation (4) gives

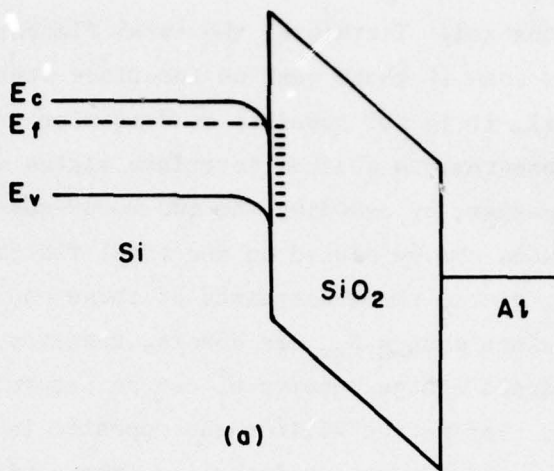
$$\ln \left[\frac{d}{dt} \Delta V_{FB} \right] = \ln \left[\frac{Jd_{ox}}{\epsilon_{ox}} (N_T S) \right] - \frac{JS}{q} t \quad (6)$$

Therefore the slope of equation (6) on a semi-log plot yields the capture cross section S . This technique is also limited to situations in which interface-state charge is a small fraction of oxide-trapped charge, that is, early in the irradiation. For hard oxides in which the amount of oxide-trapped charge is small, this may mean measuring many flatband shifts to a high degree of accuracy during the first few seconds of exposure.

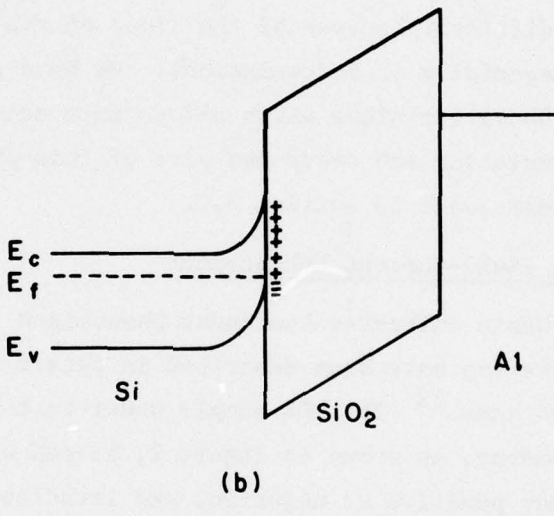
Another alternative which gives less precise results but makes measurements more feasible is to use equation (5) to determine the product $N_T S$ and then extract N_T from ΔV_{FBF} by putting upper and lower bounds on it. This can be done by measuring the flatband voltage at two points where either all the acceptor or all the donor interface states are charged.

2.2 Effect of Interface States on Measured Flatband Voltage

Consider the band diagram shown in figure 1(a). The surface is in accumulation and the Fermi level is at the conduction band edge. All acceptor interface states will be charged negatively as shown and all donors will be neutral. Thus, the total flatband shift



(a)



(b)

Figure 1. Band diagram of Si-SiO₂ MOS capacitor. (a) In accumulation, only acceptor interface-state charged; (b) in inversion, mostly donors are charged.

ΔV_{FB} will be more positive than if there were no interface states (oxide charge is positive). On the other hand, if the silicon surface is inverted as shown in figure 1(b), the Fermi level is near the valence-band edge, all donors above the Fermi level will be charged, and all acceptors neutral. Between the Fermi level and the valence band the opposite situation will prevail, but as a first-order estimate mostly

donors will be charged. Therefore, the total flatband shift ΔV_{FB} will be more negative than if there were no interface states present.

In general, it is not possible to determine from capacitance-voltage (C-V) measurements whether interface states are donors or acceptors.¹³ However, by assuming the two worst-case situations outlined above, bounds can be placed on the total flatband shift and we can determine N_T within the constraints of these bounds. For example, if all the interface states N_{SS} are donors, then for n-type silicon the actual oxide-trapped charge density N_T^+ can be determined by measuring ΔV at inversion. For p-type silicon the opposite is of course true. Measuring ΔV at accumulation and inversion from a high-frequency C-V (HFCV) plot is difficult because of the slope of the C-V curves at these points (especially at accumulation). We have devised a deep-depletion C-V (DDCV) technique which allows more accurate measurement of ΔV_{FB} at accumulation and overcomes part of this problem. This method will be discussed in section 3.2.

2.3 High Field-Current Enhancement

The basic current-enhancement phenomenon and its experimental implementation have been described in detail elsewhere and will only be outlined here.¹² The MOS sample under test is placed in a vacuum monochromator, as shown in figure 2, biased with an appropriate gate bias, either positive or negative, and irradiated with vacuum ultraviolet (VUV) light of a photon energy that is strongly absorbed* in the oxide film. The time dependence of the total current flowing through the MOS device is measured. The current measured at the initiation of radiation is just the electron or hole photocurrent flowing through the oxide. If the applied field is sufficient, eventually a

¹³G. W. Hughes, *J. Appl. Phys.* **48**, 5357 (1977).

*This is not essential, and the device may be irradiated with penetrating radiation as well.

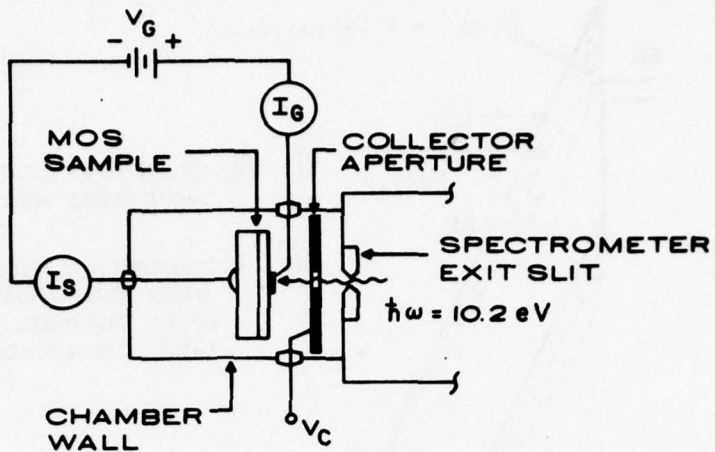


Figure 2. Experimental arrangement used for hole transport studies.

current enhancement will be observed as holes accumulate near the negatively biased electrode, and the interface field increases enough to allow Fowler-Nordheim tunneling of electrons to occur. The mechanism of current enhancement is depicted schematically in figures 3 and 4. Figure 3 shows the band diagram for SiO_2 as irradiation progresses. Initially the field throughout the SiO_2 is approximately the applied field, which must be ~ 5 MV/cm for current enhancement to occur. This is to ensure that any holes trapped at the Al interface do not perturb the field there enough to decrease the net hole generation through geminate recombination. During this time the net hole generation is constant, and the measured photocurrent does not change with time as figure 4 shows. As the density of trapped holes builds up at the silicon interface, the bands bend as shown in figure 3 until the barrier becomes thin enough for tunneling to occur. At this point, marked ① in figure 4, the total current increases as more holes are trapped and the bands are bent even further, resulting in even more tunneling current. In the absence of interface states, this situation continues until equilibrium is reached when the number of holes trapped per unit time is just balanced by the number annihilated by the tunneling electrons. This is marked ② in figure 4 as the current approaches

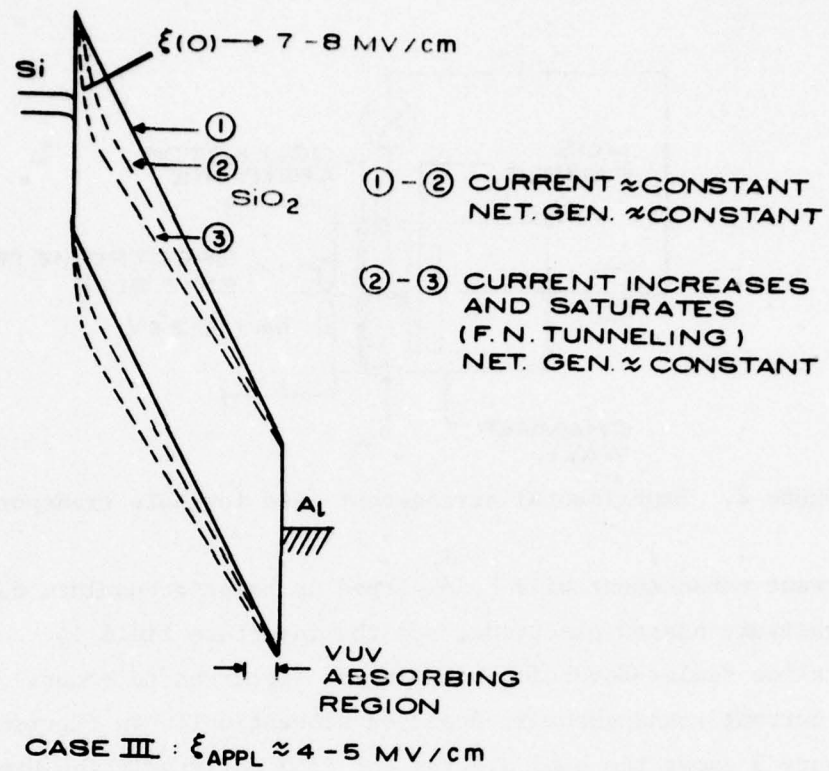


Figure 3. Energy band diagram of an Si-SiO₂ MOS structure with high applied field.

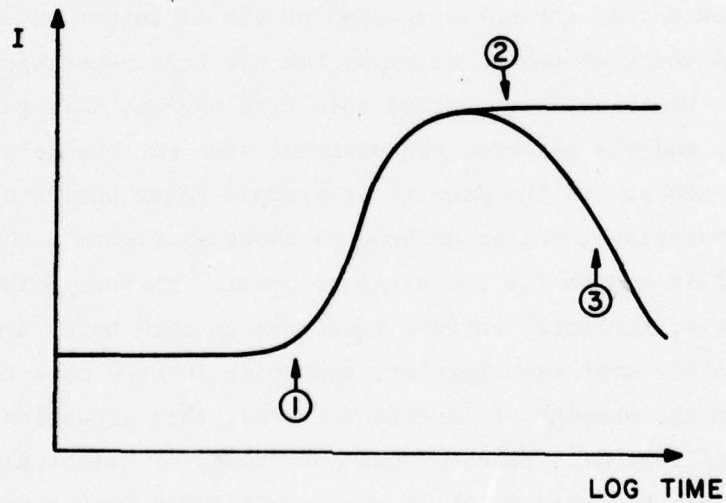


Figure 4. Behavior of measured current vs time under bias conditions shown in fig. 3. Numbers refer to discussion in text.

saturation. In some samples, instead of saturating, the current actually begins to decrease as time goes on. One might speculate that this is due to a decrease in the net number of trapped holes as electrons tunneling in from the silicon annihilate them. However, this would have a self-limiting effect since as the net hole density decreases, the interface field and hence the tunneling current would decrease until equilibrium was reached. Actually, equilibrium would be established before the current had a chance to decrease and situation ② would prevail. The most probable explanation for this decreasing current phenomenon is that acceptor-type interface states are generated near the interface and partially compensate the field enhancement due to hole trapping. This hypothesis is illustrated in figure 5. Here we show the band diagram at the Si-SiO₂ interface under three different conditions. Condition I shows the SiO₂ conduction band edge under an oxide field of 5 MV/cm with no oxide charge or interface states. Condition II includes a positive sheet of oxide charge of $5 \times 10^{12} \text{ cm}^{-2}$ 50 Å from the Si-SiO₂ interface, and condition III includes both the positive oxide charge and a negative sheet of interface states 10 Å from the interface of the same magnitude as the oxide charge. The location and magnitude of the positive charge is reasonable and is based upon measurements of charge centroids^{11,14} and our current-enhancement data. The location of the interface-state centroid at 10 Å from the silicon interface is not unreasonable especially for midgap states.¹⁵ The magnitude of this charge is based upon the deep-depletion C-V measurements shown below.

¹⁴R. J. Powell and G. W. Hughes, "Radiation and Charge Transport in SiO₂," Annual Report prepared under Contract N00014-74-C-0185 for Office of Naval Research, January 1975.

¹⁵F. P. Heiman and G. Warfield, IEEE Trans. Electron. Devices ED-12, 167 (1965).

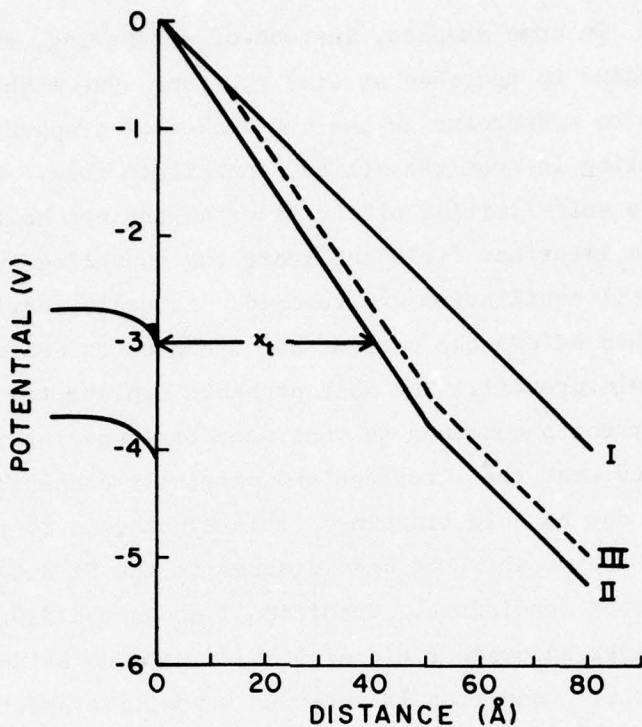


Figure 5. Band diagram of Si-SiO₂ MOS interface showing the effect of positive and negative sheet on band bending and tunneling distance. Roman numerals refer to discussion in text.

In condition I, no current enhancement results because the tunneling distance $x_t \approx 60 \text{ \AA}$. In condition II, the positive sheet charge increases the interfacial field to 7.5 MV/cm, and decreases the tunneling distance to 40 \AA allowing large enhancement currents to flow. In condition III, the negative interface-state charge compensates the positive oxide charge and the tunneling distance x_t increases to $\approx 42 \text{ \AA}$. Since the tunneling current depends exponentially upon barrier width, this results in a decrease in current by at least an order of magnitude.¹²

Current enhancement is also a very useful tool for probing the hole traps at the Al-SiO₂ interface where there is no counterpart to

flatband shift measurements. The current enhancement at this interface is solely a function of the applied field and trap density. Interface states do not exist here, so that the interpretations are simplified. In section 4.2 we present some interesting results using this technique.

3. EXPERIMENTAL METHODS

3.1 Sample Preparation

Oxide films were thermally grown on n- and p-type 5 to 10 ohm-cm (100) silicon slices by three different processes. These processes are summarized in table I.

TABLE I. PROCESSING CONDITIONS

Oxidation Process	Oxidation Temperature (°C)	Anneal Temp (15 min)	Nominal Oxide Thickness (Å)
Dry (p-type)	900 1000 1150	Half annealed in Ar at 800°C, half unannealed	750
Pyrogenic Steam (100%) (n-type)	875	900°C to 1100°C in He	1000
Hybrid (30-min 100% pyrogenic with 3% HCl steam (60-min dry O ₂ (n-type)	925	925°C <i>in situ</i> in N ₂	750

Pyrogenic steam is nothing more than steam produced by burning hydrogen inside the furnace tube. With adjustment of the ratio of H₂ to O₂, the steam content can be varied from 0 to 100%. The advantages of this method are (1) the percentage steam can be controlled accurately, (2) the purity of the steam is determined solely by the purity of the gases, and (3) the steam can be quickly and easily shut on and off, making hybrid oxides possible.

All of these wafers were metallized with 1-mm-diameter semi-transparent aluminum dots approximately 100 Å thick. The aluminum was evaporated from an In Source[®] induction-heated crucible source and in all cases resulted in less than 0.1-V shift under a standard bias-temperature C-V test (CVBT; +10 V at 300°C for 5 min).

For comparison purposes all wafers used in the capture cross-section study were also irradiated with 1-MeV electrons under 1-MV/cm positive bias to a dose of 10^6 rad. The results of this test are shown in figures 6, 7, and 8. All flatband shifts are normalized by a square law thickness dependence to 750 Å. As the figures show, some of the oxides are relatively hard and some of them, not being grown by an optimum process, are very soft. This wide range of radiation sensitivities is desirable in that it provides us with a wide range of process-induced trapping situations for study. The inclusion of a hard oxide from each of the three processes also provides us with a benchmark for comparison of the other oxides.

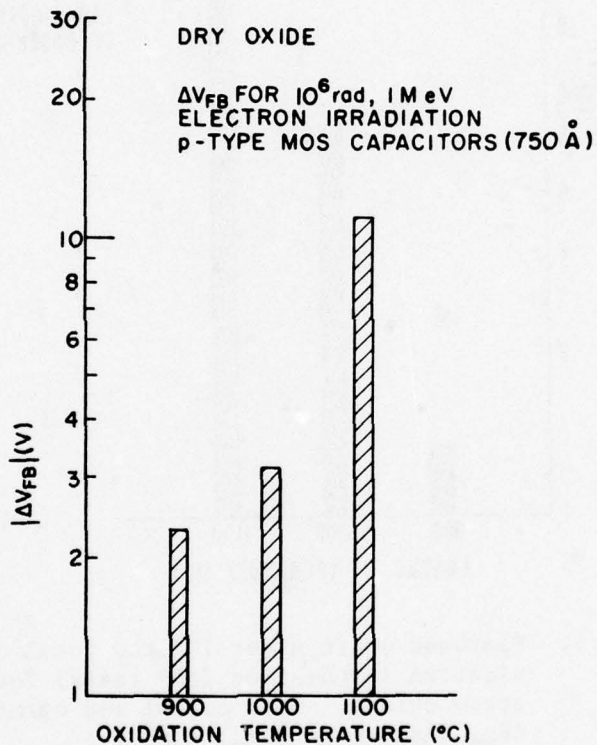


Figure 6. Flatband shift after 10^6 rad total dose 1-MeV electron irradiation (10⁴ rad/s) for dry oxides.

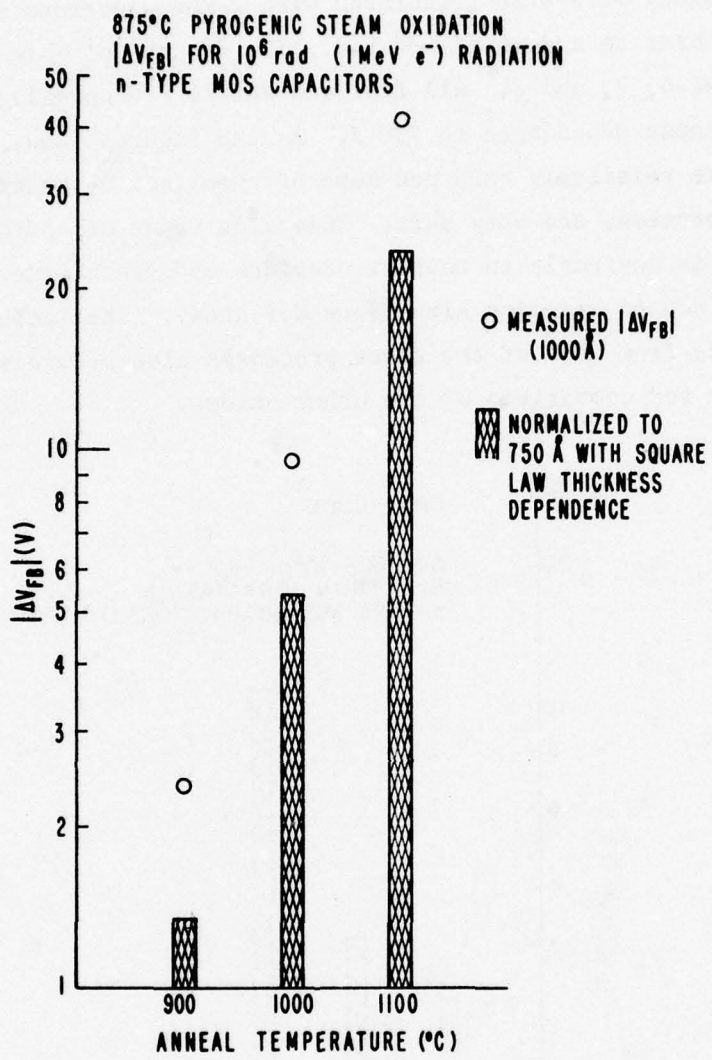


Figure 7. Flatband shift after 10^6 rad total dose 1-MeV electron irradiation (10^4 rad/s) for pyrogenic steam oxides. Both actual and normalized ΔV_{FB} data shown ($\Delta V_{FB} \propto d_{ox}^2$).

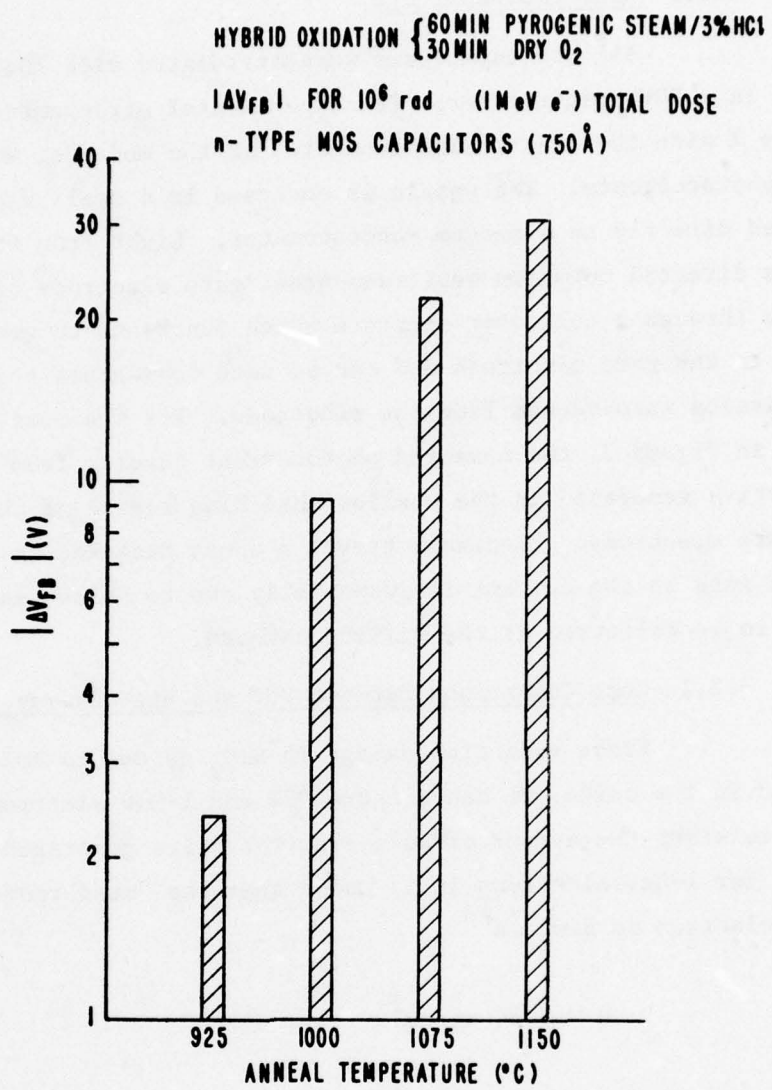


Figure 8. Flatband shift after 10^6 rad total dose 1-MeV electron irradiation (10^4 rad/s) for hybrid oxides.

3.2 Measurement Techniques

3.2.1 Hole Photocurrents

All MOS capacitors were irradiated with 10.2-eV VUV light in a VUV spectrometer. The experimental arrangement is shown in figure 2 with the electronics connected in the mode for measuring the hole photocurrents. The sample is enclosed in a small vacuum chamber coupled directly to a vacuum monochromator. Light from the monochromator is directed onto the semitransparent gate electrode of the MOS sample through a collector aperture which functions to confine the light to the gate electrode and can be used to measure the magnitude of emission into vacuum from the electrode. For the bias polarity shown in figure 3, the measured photocurrent results from electron-hole pairs generated in the shallow absorbing region of the SiO_2 near the gate electrode. Electrons travel a short distance to be collected at the gate so the current is essentially due to holes traversing the oxide to be collected at the silicon cathode.

3.2.2 Dose Comparison Between VUV and High Energy Irradiation

Since radiation damage in SiO_2 is due to holes being trapped in the oxide, we can compare VUV and 1-MeV electron irradiation by calculating the number of hole-electron pairs generated per second.

For 1-MeV electrons it is known that the "mean range" of a 1-MeV electron in SiO_2 is¹⁶

$$R = 3.84 \text{ mg/cm}^2 \quad (9)$$

The density of SiO_2 is 2.3 g/cm^3 so that the actual absorption depth is

$$L_A = 0.169 \text{ cm} \quad (10)$$

¹⁶L. Katz and A. S. Penfold, *Rev. of Modern Physics* 24, 28 (1952).

Defining $\beta = \frac{L_A}{E_s}$ where $E_s = 1$ MeV, then,

$$\beta = 1.69 \times 10^{-7} \text{ cm/eV} \quad (11)$$

Assuming a pair formation energy E_p , the length required to create one electron-hole pair is βE_p . The total number of electron-hole pairs/cm² created in an oxide of thickness d_{ox} after a dose of Φ rad is then

$$N_p = \alpha \Phi \frac{d_{ox}}{\beta E_p} \quad (12)$$

where $\alpha = 3 \times 10^{-7}$ MeV electrons/cm²/rad.

Srour et al.¹⁷ have estimated $E_p \approx 19$ eV. Therefore, for a 750-Å-thick oxide and a dose of 10^6 rad,

$$N_p = 6.96 \times 10^{13} \text{ cm}^{-2} \quad (13)$$

For VUV irradiation, Powell has shown that the initial hole photocurrent and thus the quantum yield Y saturates with Y near 100% as the oxide field approaches 5 MV/cm because of the reduction of geminate recombination.¹²

For the light intensity and electrode area that we use, we find the hole photocurrent at 5 MV/cm is typically

$$J_{ph} \approx 5.1 \times 10^{-8} \text{ A/cm}^2 \quad (14)$$

Thus, the number of electron-hole pairs created by the VUV per cm² per second is

$$\frac{J_{ph}}{q} = 3.18 \times 10^{11} \text{ s}^{-1} \text{ cm}^{-2} \quad (15)$$

The total number for t in seconds is then

$$N_p = \frac{J_{ph}}{q} t \quad (16)$$

¹⁷J. R. Srour, O. L. Curtis, and K. Y. Chiu, *IEEE Trans. Nucl. Sci.* NS-21, 73 (1974). For analysis of data in preceding reference, see G. A. Ausman, Jr. and F. B. McLean, *Appl. Phys. Letters* 26, 173 (1975).

So from equation (13) and (16) we find $t \approx 218$ s for an equivalent 1-Mrad VUV dose.

3.2.3 Deep-Depletion C-V Measurements

Flatband shifts during irradiation were measured by both a high-frequency C-V (HFCV) technique and a deep-depletion C-V (DDCV) technique. In the high-frequency technique, the capacitor is irradiated for a length of time at a positive bias, the radiation is removed, and a 1-MHz HFCV curve is taken. The whole procedure takes about 20 s. In the DDCV technique, a bias is applied during the irradiation as shown in figure 9. With a small sampling resistor, R_S , the current is calculated by measuring the voltage $V_S(t)$ as shown in figure 9. When a DDCV measurement is desired, the bias is rapidly swept down to a preset negative voltage and back, the whole sweep taking about 100 μ s. During this time the UV can be either on or off as it does not affect the measurement. The method is similar to a quasi-static C-V measurement except that the sweep rate of the ramp voltage is very high. Under steady-state conditions, the capacitor is biased far into accumulation at $+V_B$. At the moment the DDCV curve is needed, a high sweep-rate negative-going ramp is initiated which sweeps to $-V_I$ and then retraces at the same rate back to $+V_B$. If α is the sweep rate of the ramp, then, neglecting R_S , the current through the capacitor is

$$I = C(V_g) \frac{dV_g}{dt} = \alpha C(V_g) \quad (17)$$

and

$$V_S = IR_S = \alpha R_S C(V_g) \quad (18)$$

Time is related to V_g through the relationship $V_g = \alpha t$ so that the time scale can be quickly converted to a voltage scale.

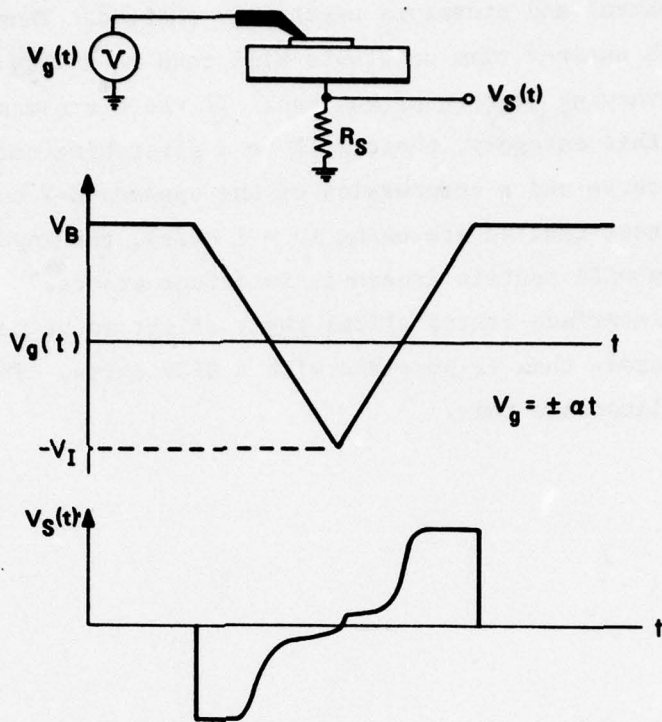


Figure 9. Deep-depletion C-V measurement technique showing circuit connections and voltage waveforms.

Without interface states, the above system gives an accurate replica of a deep-depletion C-V curve. The majority carriers are in equilibrium with the ramp voltage as long as the sweep time is long compared with the geometrically modified dielectric-relaxation time of the MOS capacitor.¹⁸ The minority carriers are "frozen-out" for moderate to high slew rates. When interface states are present, the response of the capacitor is slightly different. Interface states with time constants long compared with the sweep time will be "frozen in" with the Fermi level at the conduction band point. That is, donors

¹⁸ G. W. Hughes and R. M. White, *IEEE Trans. Electron. Devices* ED-22, 945 (1975).

will be neutral and acceptors negatively charged. Those interface states with shorter time constants will tend to follow the voltage ramp with varying degrees of success. If there are many interface states in this category, there will be a stretching out of the down-sweep C-V curve and a compression of the upsweep C-V curve.¹⁹ For the sweep rate that we are using ($\alpha = 1$ MV/s), the lower 0.7 eV of the bandgap will contain frozen-in interface states.²⁰ This freezing-in of the interface states allows their effect to be measured much more accurately than is possible with a HFCV curve. The data in section 4.1 illustrate this.

¹⁹ J. G. Simmons and L. S. Wei, *Solid State Electronics* 16, 53 (1973).

²⁰ S. M. Sze, *Physics of Semiconductor Devices* (John Wiley & Sons, New York, 1969), p. 455.

4. MEASURED HOLE CAPTURE CROSS SECTION AND TRAP DENSITIES

4.1 Interpretation of ΔV_{FB} vs t Data

Using the techniques described in section 3, we irradiated MOS capacitors on the oxides shown in table I and measured the flat-band shifts as a function of time. From these data, the capture cross section and trap density were determined.

At the beginning of the irradiation the initial probability of capture P_{co} is given by

$$P_{co} = N_T S \quad (19)$$

From equation (5) this is

$$P_{co} = \frac{C_{ox}}{I_0} \frac{d}{dt} [\Delta V_{FB}]_{t=0} \quad (20)$$

where C_{ox} is the actual oxide capacitance and I_0 is the initial photo-current.

For $t \ll q/JS$, equation (3) shows that

$$\Delta V_{FB} \sim \frac{I_0}{C_{ox}} P_{co} t \quad (21)$$

This equation can safely be used to measure P_{co} directly as long as the measured ΔV_{FB} versus t is linear in t . For example, in our experiments it is difficult to determine exposures accurately for less than 1 s, and it becomes increasingly difficult to resolve small flat-band shifts for very short exposures. Consequently, our measurement technique consists of the following procedure. The sample is exposed for 1 s, a DDCV curve taken, the sample allowed to relax for 60 s, and a DDCV curve is taken again. This allows any transporting charge to move completely through the oxide. The sample is exposed again for another 1 s and the whole process repeated. An example of the resulting

flatband shifts before and after relaxation is shown in figure 10. This is an 875°C pyrogenic oxide annealed at 900°C in helium. The bias during irradiation is +5 MV/cm. (This particular bias was used during most of the measurements because it is the bias needed to interpret the current enhancement data.) The probability of capture was measured for other biases and was found to be bias-dependent. This will be discussed below. This particular sample had about 0.04-V shift due solely to transporting charge which disappeared after the capacitor was allowed to relax. Other samples showed less of a discrepancy between the initial and relaxed ΔV_{FB} . Note also that the slope of ΔV_{FB} versus t is 1.0 on a log-log scale which validates the assumptions made for equation (21). From this figure and equation (21), we find

$$P_{co} = N_T S = 0.02.$$

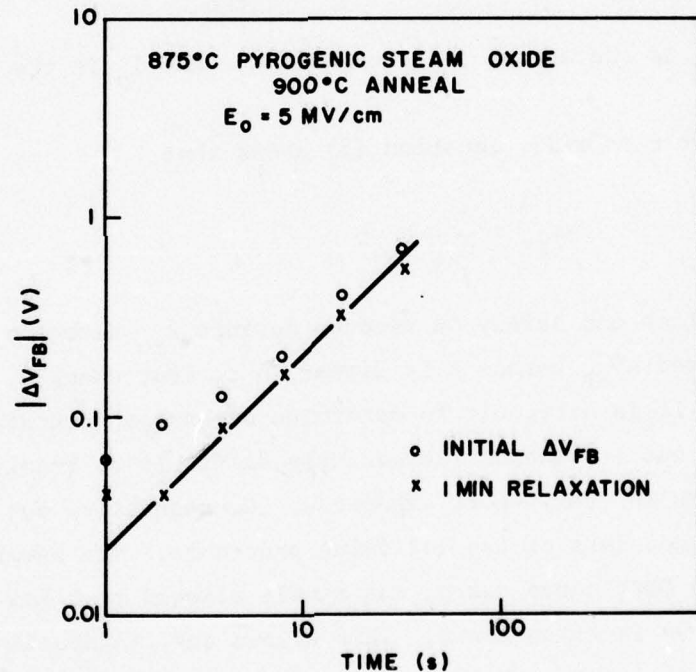


Figure 10. Initial $|\Delta V_{FB}|$ vs t data for pyrogenic steam oxide annealed at 900°C, showing relaxation effect and resulting unity slope line.

After the probability of capture is measured, what remains to be determined is N_T or S from the ΔV_{FB} versus t data. As explained above, because of the relative inaccuracy in our measurement technique, it is not possible to use equation (6) to measure the capture cross section S . Instead, we measured ΔV versus t by both HFCV and DDCV techniques and determined bounds on ΔV_F from these measurements. Figure 11 shows these measurements for the same sample as in figure 10. This figure contains three sets of data, the DDCV data measured from accumulation (+5 MV/cm), and the HFCV data measured at flatband and inversion. As the figure shows, for $t > 250$ s, the DDCV curve begins to deviate from the HFCV curve and eventually reverses. The deviation between the curves shows that interface states are being created between the flatband Fermi level and silicon conduction band. However, it is not possible to determine whether these states are donors or acceptors.¹³ The reversal of the DDCV curve implies one of two things. (1) The oxide trapped charge N_T^+ is being annihilated by electrons tunneling in from the silicon under high fields (see fig. 3). This must be accompanied by an increase in the number of donor interface states above the flatband Fermi level E_F which must compensate both the annihilated N_T^+ and all acceptor N_{SS} below E_F . (2) The net oxide-trapped charge N_T^+ does not decrease with time but the number of acceptor N_{SS} throughout the bandgap increases and becomes greater than N_T^+ (see section 2.2).

For the reasons given in section 2 we believe the second scenario is the most probable one, but in either case the reversal can be used to set a lower bound on N_T , the number of fillable traps. The Fermi level is at the conduction band when the DDCV measurement is initiated, so that in either case only acceptor interface states are charged and ΔV_{FB} due to N_T is at least as large as the maximum shown.

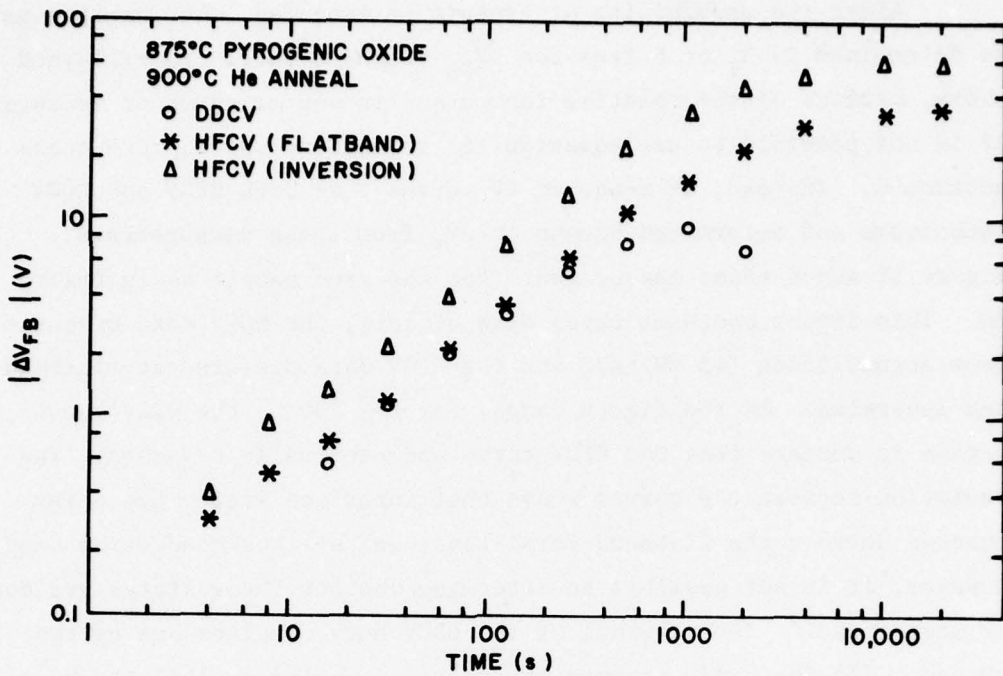


Figure 11. Complete $|\Delta V_{FB}|$ vs t data for pyrogenic steam oxide annealed at 900°C showing differences between DDCV and HFCV techniques. 5-MV/cm bias.

The upper limit on N_T is of course determined by the saturated C-V shift at inversion. Here the Fermi level is near the silicon valence band, all the donors above E_F are charged positively, and any acceptors between E_V and E_F are charged negatively. Presumably, the net interface charge in this case would be positive. This being the case, the ΔV due to N_T , the number of fillable traps, is no larger than that measured at inversion.

These two cases give us limits on N_T through the equation

$$N_T = \frac{\epsilon_{ox}}{qd_{ox}} |\Delta V_F| \quad (22)$$

where ϵ_{ox} and d_{ox} are the permittivity and thickness of the SiO_2 and q is the magnitude of the electronic charge. From the upper and lower limit on N_T , lower and upper limits on S can be computed from equation (19). This was done for some of the oxides shown in table I for applied oxide fields E_o of 1, 3, and 5 MV/cm. The data from these measurements are shown in appendix A. The results of the capture cross section and trap density calculations are shown in figures 12, 13, and 14 for $E_o = 1$ MV/cm. While capture cross-section data do not provide any definitive answers about the nature of hole traps, such data can be useful for comparing oxides of different degrees of hardness. For the oxides grown for this study, the degree of hardness ranges from very hard to very soft depending upon the particular process used. It would be useful then to know if the capture cross sections for the very hard and very soft oxides are quite different, suggesting a different hole trap, or if they are the same, suggesting perhaps only a difference in trap density.

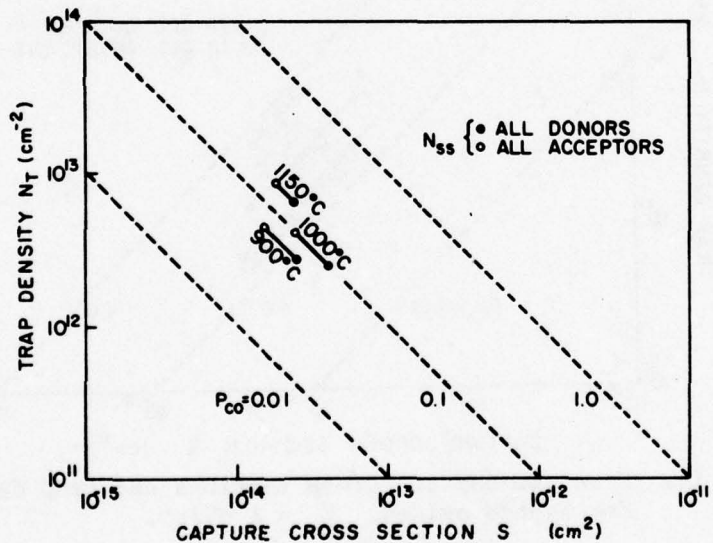


Figure 12. Measured capture cross sections and trap densities for unannealed dry oxides. $E_o = 1$ MV/cm.

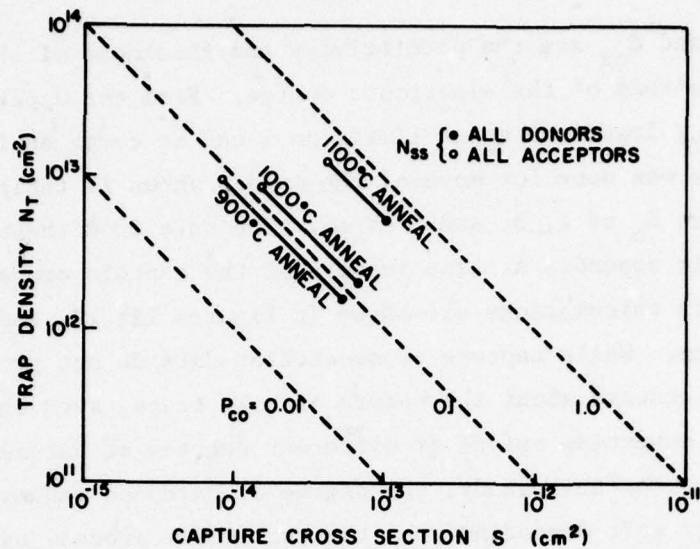


Figure 13. Measured capture cross sections and trap densities for pyrogenic steam oxides. $E_0 = 1 \text{ MV/cm.}$

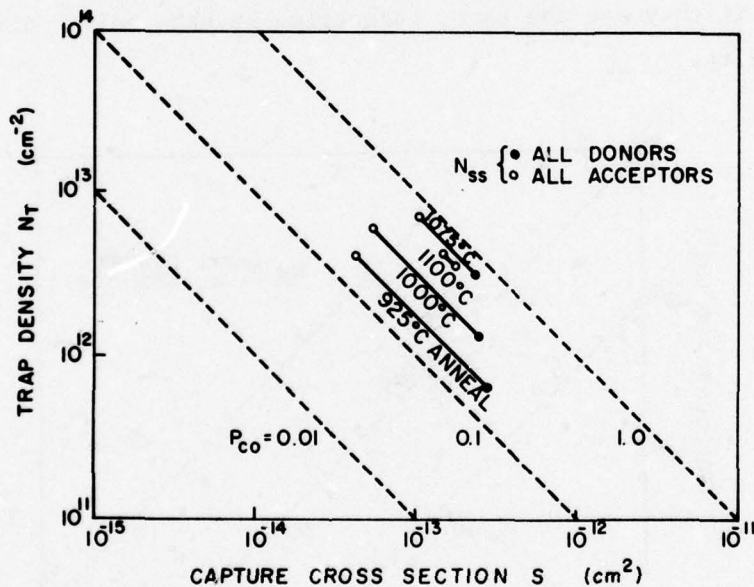


Figure 14. Measured capture cross sections and trap densities for hybrid oxides. $E_0 = 1 \text{ MV/cm.}$

For the unannealed dry oxides shown in figure 12, it can be seen that the spread in N_T is relatively small, indicating not too many interface states. The initial probability of capture is ~ 0.1 for all three oxidations, even though the high-energy 1-Mrad radiation data in figure 6 show a factor of 5 difference in ΔV_{FB} between 900° and 1000°C hard oxides and the 1150°C soft oxide. In addition the DDCV data shown in appendix A indicate no current reversal and therefore few acceptor interface states. However, the spread in N_T indicates some interface states present which would suggest that they are mainly donors. The capture cross section S for these oxides is $\sim 5 \times 10^{-14} \text{ cm}^2$.

The pyrogenic steam oxides in figure 13 show a much wider spread in N_T indicating many more interface states than the dry oxides. The DDCV data in the appendix show a current reversal, indicating acceptor interface states present. Since we know nothing about the donors, we cannot say exactly where on the constant P_{co} lines the data actually lie. Here the capture cross section for the oxide traps is less certain but appears to lie between 5×10^{-14} and 10^{-13} cm^2 for all the oxides taken as a whole. As figure 7 shows, the ΔV_{FB} for high-energy irradiation of these samples ranges over more than an order of magnitude. The 900°C annealed oxide shows a very acceptable 1.3-V shift in figure 7, but as figure 13 shows, the P_{co} is not much different from the soft 1000°C annealed oxide. The differences in hardness shown in figure 7 are probably due mainly to interface states.

The pyrogenic hybrid oxides shown in figure 14 are somewhat anomalous when compared with the dry and steam oxides of figures 13 and 14. The range of possible capture cross sections for the dry and steam oxides overlap enough that we might conclude that the trap involved in all cases is the same and that only the density of traps and interface states are different between the oxides. With the hybrid oxides, however, it becomes increasingly difficult to stretch this argument. Here it appears that a trap with $S \sim 2 \times 10^{-13} \text{ cm}^2$ could explain all the hybrid data. This is four times larger than that

assumed for the dry oxides. The significant thing about the hybrid data is that the main difference between the 925°C annealed hard oxide (see fig. 8) and the soft oxides is the density of traps and interface states. The capture cross section ranges for all hybrid oxides overlap completely. Here again, as shown for the hard pyrogenic steam oxide, the hard hybrid oxide has a substantial number of interface states. The data in the appendix show that many of these are acceptors, and they therefore must provide a certain amount of compensation for the trapped holes.

The range of uncertainty in N_T and S is delineated in figures 12, 13, and 14. The uncertainty in P_{co} is not shown here but could be as high as $\pm 50\%$ for the worst case. Even at this extreme it is not possible to reconcile all oxides measured and show them as having only one capture cross section. What is significant, however, is that all the dry oxides and the 900° to 1000°C annealed pyrogenic oxides have traps with about the same cross section. This suggests that hole traps in wet and dry oxides are the same. The differences in hardness measured could then be explained by differences in trap density and interface state density alone. The oxides that do not fit in this category may have some sort of impurity-related trap in addition to the *intrinsic* trap of the hard oxides. The hybrid oxides were in fact grown in an ambient of 3% HCl which may very well change the structure of the oxide as well as the trap capture cross section.

The capture cross sections of these hole traps were measured with an oxide field E_o of 1 MV/cm (which is the normal bias field) and $E_o = 5$ MV/cm (which is the field used for current enhancement). Much to our surprise, the capture cross section was found to be field-dependent so that $S \propto E_o^{-1}$. This is shown in figure 15 for the 1000°C dry oxide (unannealed). We have actually shown P_{co} , the initial probability of capture here, but, as shown in figure 16, ΔV_{FBF} is field-independent, so it is actually S which is field-dependent in P_{co} . The

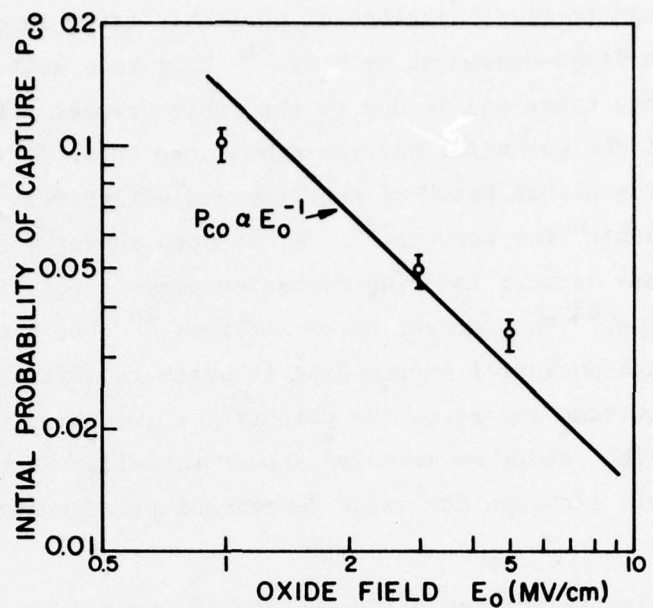


Figure 15. Field dependence of initial probability of capture for unannealed 1000°C dry oxide.

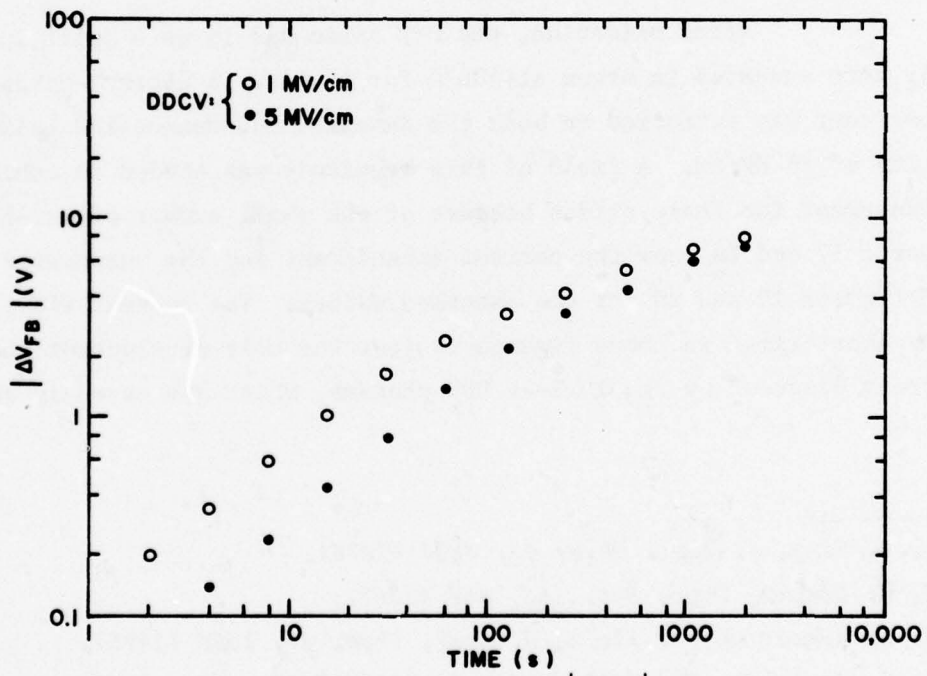


Figure 16. Field dependence of $|\Delta V_{FB}|$ vs t data for unannealed 1000°C dry oxide.

electron capture cross sections of coulombic traps in SiO_2 have been shown to be field-dependent by Ning.²¹ This is a well known phenomenon for coulombic traps and is due to the Poole-Frenkel effect or field lowering of the potential barrier around the trap.²² This decreases the "sticking probability" of the trap and effectively decreases the "critical orbit" for capture.²¹ It has been shown by Arnett and Klein that the same barrier lowering mechanism plays a role in capture by neutral traps.²³ They argue, after Jonscher,²⁴ that a neutral trap has a short-range potential surrounding it which is affected by the applied field in the same way as is the potential surrounding the coulombic trap. All the oxides we measured showed a similar decrease in S with applied field although the exact functional relationship has not been determined.

4.2 Interpretation of Current-Enhancement Data

4.2.1 Dry Oxides

After oxidation, the dry oxide wafers were split in half; half were annealed in argon at 800°C for 15 min. A current-enhancement experiment was performed on both the annealed and unannealed oxide fields of $\pm 6 \text{ MV/cm}$. A field of this magnitude was needed to achieve enhancement for these oxides because of the small number of oxide traps. Figures 17 and 18 show the current enhancement for the unannealed oxides and figures 19 and 20 for the annealed oxides. The current flowing for very short times in these figures is just the hole or electron photo-current produced by the 10.2-eV VUV photons, which are strongly absorbed

²¹ T. H. Ning, *J. Appl. Phys.* **47**, 3203 (1976).

²² J. G. Simons, *Phys. Rev.* **155**, 657 (1967).

²³ P. C. Arnett and N. Klein, *J. Appl. Phys.* **46**, 1400 (1975).

²⁴ A. K. Jonscher, *Thin Solid Film* **1**, 213 (1967).

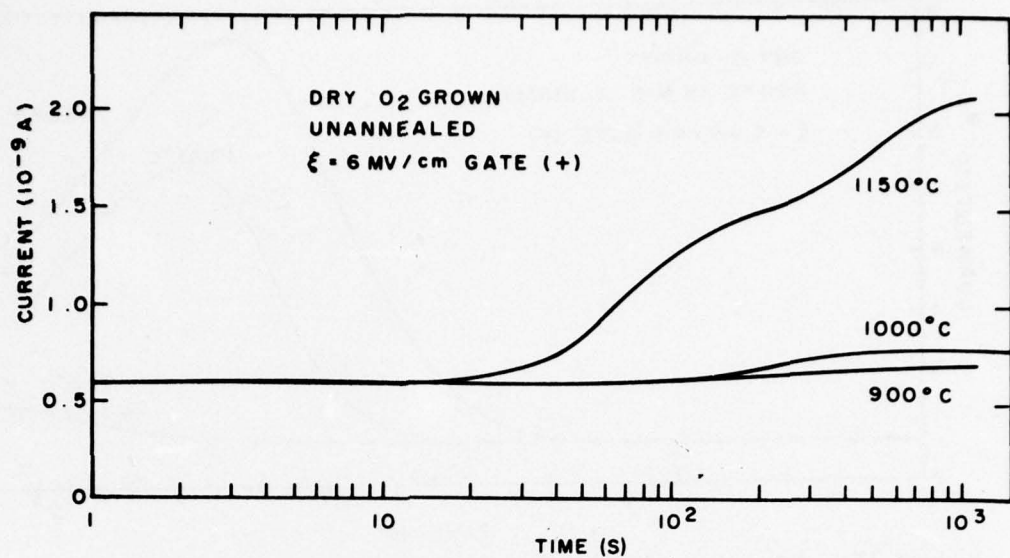


Figure 17. Time dependence of current during VUV irradiation for dry O₂-grown samples with different growth temperatures. Positive gate bias was used to produce an average field of 6 MV/cm in the oxide. The photon energy was 10.2 eV and SiO₂ absorbed photon flux was $4 \times 10^{11} \text{ cm}^{-2} \text{ s}^{-1}$.

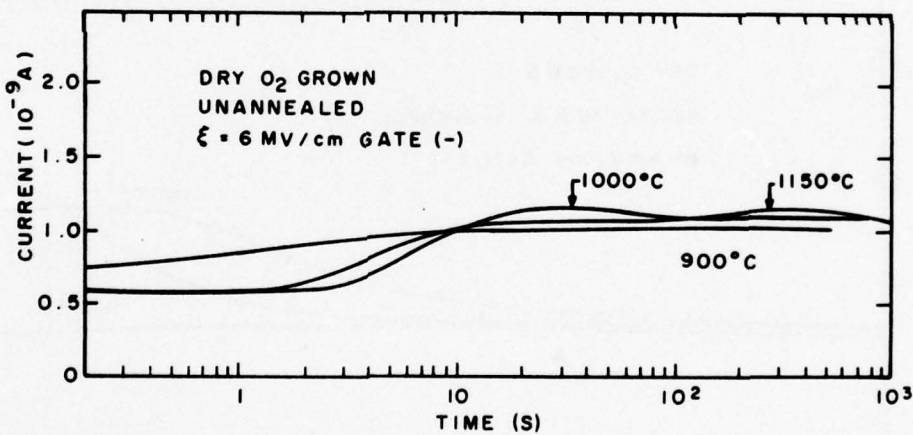


Figure 18. Time dependence of current during VUV irradiation for dry O₂-grown samples with different growth temperatures. Negative gate bias was used. Other conditions were the same as in figure 17.

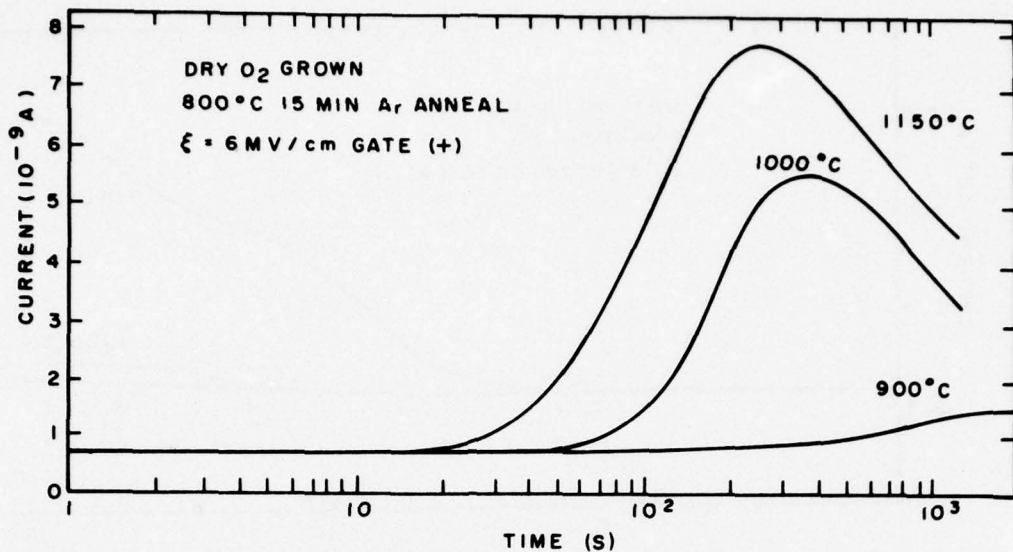


Figure 19. Time dependence of current during VUV irradiation for dry O₂-grown samples which were annealed in argon at 800°C for 15 min. Positive gate bias was used to produce an average oxide field of 6 MV/cm. The photon energy was 10.2 eV and the SiO₂ absorbed photon flux was $4 \times 10^{11} \text{ cm}^{-2} \text{ s}^{-1}$.

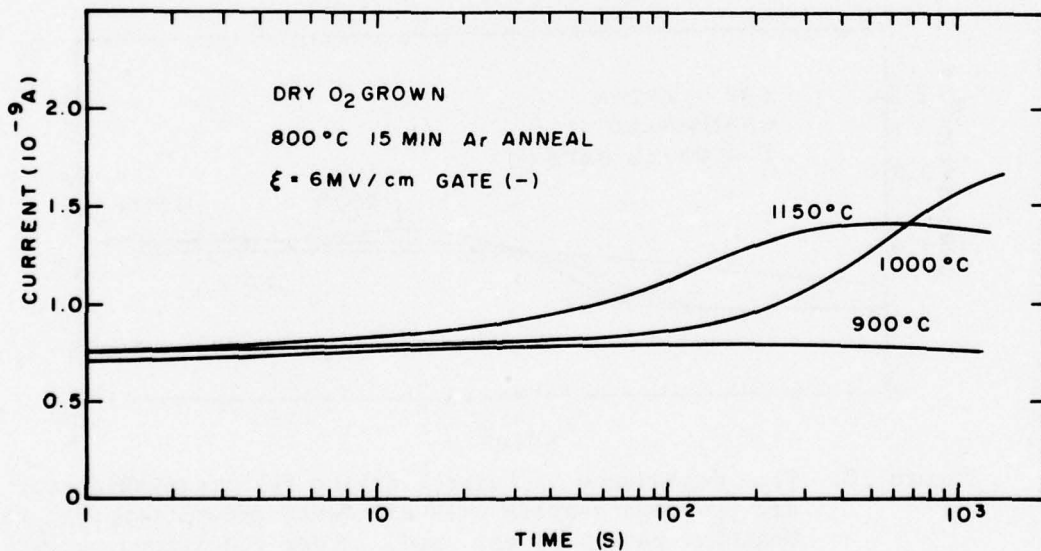


Figure 20. Time dependence of current during VUV irradiation for dry O₂-grown samples which were annealed in argon at 800°C for 15 min. Negative gate bias was used. Other conditions are the same as in figure 19.

in the SiO_2 near the gate electrode. When sufficient space charge accumulates to raise the interface field close to 7 MV/cm, the current increases. The curves in figure 17 show the time dependence of total oxide current for samples with three different growth temperatures. It is apparent from these results that the smallest number of traps is obtained for the lowest growth temperature, 900°C, and the number increases with temperature. The curves in figure 18 depict the current-time characteristics of the unannealed samples under negative gate bias. In this case, holes generated in the shallow absorbing region near the gate are swept out to the gate. Some, however, are trapped in this region, and the accumulating space charge enhances the field at the gate until the current is enhanced by electron tunneling from the gate into the oxide. This experiment provides us with a method of estimating and comparing the number of hole traps effective in enhancing the field at the gate. A surprising fact is that for both the 900° and 1000°C samples the current enhancement is actually larger under negative gate bias than with positive bias. One might be tempted to suggest that in these samples the hole trapping is distributed throughout the oxide with the centroid lying somewhat closer to the gate for the 900° and 1000°C samples. However, that this is definitely not the case is readily proven. First, the trapping in the negative bias case must be almost entirely within 200 Å of the gate electrode because the absorption depth of the 10.2-eV light is only about 100 Å. Second, the capacitance-voltage flatband shifts for negative bias are seven to eight times smaller than for positive bias, as illustrated in figure 21, so we must conclude that the charge is very near the gate electrode following negative bias irradiation.

Charge trapped near the gate will have little effect on the current enhancement and flatband shift under positive bias, and charge is mostly near the $\text{Si}-\text{SiO}_2$ interface following positive bias irradiation. Using these facts, we can estimate the location of charge trapped near the gate following negative bias irradiation. The results of

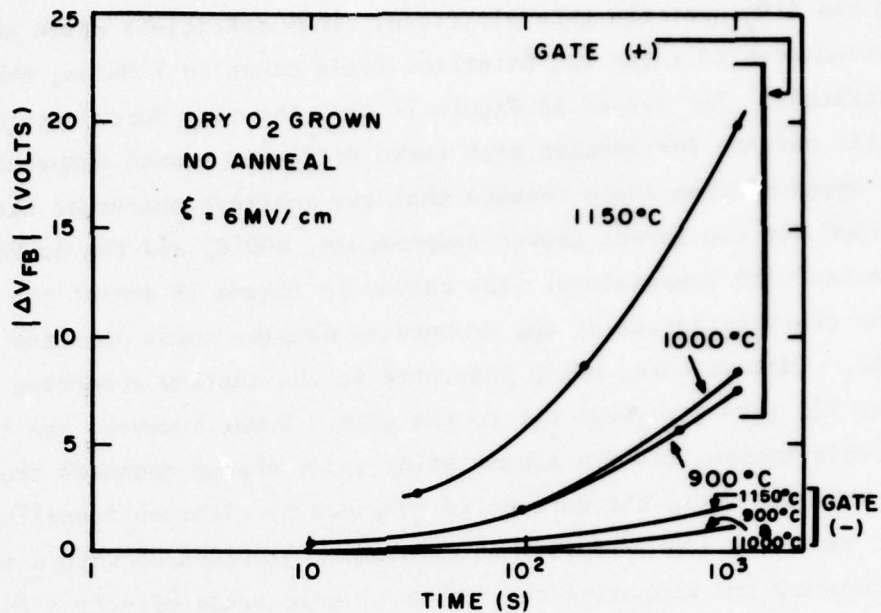


Figure 21. Flatband shift vs time during irradiation with positive and negative bias for unannealed dry oxides.

figures 17 and 18 indicate that for the 900° and 1000°C samples, comparable amounts of charge are trapped near the silicon and aluminum. Since the $|\Delta V_{FB}|$ for the two cases differs by a factor of ~ 7 , the charge centroid for the negative bias case must be ~ 7 times closer to the gate than for the positive bias case. This places the centroid within about 100 Å of the Al-SiO₂ interface. The above argument assumes that the trapped charge is as effective in producing current enhancement as it is in producing flatband shift. This is not true when charge is trapped extremely close to the interface (within ~ 30 Å).²⁵

²⁵R. J. Powell, "Radiation and Charge Injection in Al₂O₃ Using New Techniques," Final Report No. AFGL-TR-76-0017 for Air Force Geophysics Laboratory, January 1976.

Presented in figures 19 and 20 are curves which summarize the experimental results for VUV current enhancement experiments on the set of samples which was annealed in argon following oxidation. Focusing on figure 19, we first observe the greatly increased current enhancement compared with the unannealed samples in figure 17 (note scale differences between these figures). This result indicates that the argon anneal has markedly increased the number of oxide traps which are effective in producing current enhancement and flatband shifts. This statement is borne out by the flatband shift data shown in figure 22. The shifts here are in every case significantly larger than those of the unannealed oxides (fig. 21). The second observation is that the current begins to decrease for the 1000° and 1150°C oxides at about 250 to 300 s. As explained in section 2.3, this is due to a large increase in acceptor interface states. (Note that only acceptors are charged in positive bias current enhancement.)

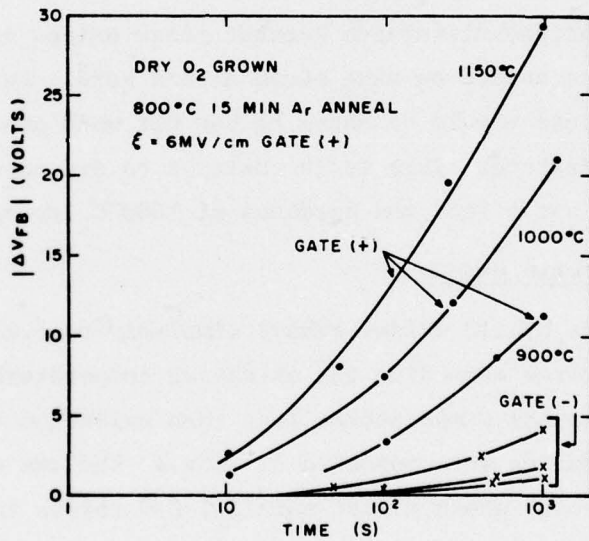


Figure 22. Flatband shift vs time during VUV irradiation with positive and negative gate bias for argon-annealed oxides.

A comparison of figures 20 and 18 shows that the trapping near the gate electrode has not been significantly increased by the argon anneal. These results suggest that the anneal does not appreciably change the basic trap structure of the oxide bulk and near the gate electrode, but does modify it markedly near the Si-SiO₂ interface.

4.2.2 Pyrogenic Steam Oxides

In addition to the 900°, 1000°, and 1100°C annealed steam oxides, oxides were also annealed at 850°, 950°, and 1050°C for current-enhancement measurements. Figure 23 shows these results. It is interesting to note here that the minimum current enhancement occurs at 1000°C and the minimum flatband shift occurs at 900°C for high energy irradiation (see fig. 7) and VUV irradiation up to 500 s (fig. 24). It may be that acceptor interface states compensate the trapped holes for current enhancement even before the current starts rising. For hard oxides such as these, a higher applied field is needed to see the effects of hole traps first.

One important difference between steam oxides and dry oxides is that anneals are needed to make steam oxides hard. Furthermore, the anneal temperature should be equal to but not much greater than the oxidation temperature. This is in contrast to dry oxides where anneals below 800°C do not affect the hardness of 1000°C dry oxides at all.

4.2.3 Hybrid Oxides

The hybrid oxides behave similarly to steam oxides for anneal temperatures exceeding the oxidation temperature. (We do not have data for anneal temperatures less than oxidation temperatures since all the oxides were annealed *in situ*.) The one exception is the 1150°C anneal which shows almost parallel C-V shifts indicating very little interface state generation. This is supported by the DDCV and HFCV shifts as shown in figure 25. All the other anneals show acceptor interface state generation as reflected in the reversal of the DDCV ΔV_{FB} . Figure 26 shows the current-enhancement characteristic for these oxides, and figure 27 shows the ΔV_{FB} vs t data.

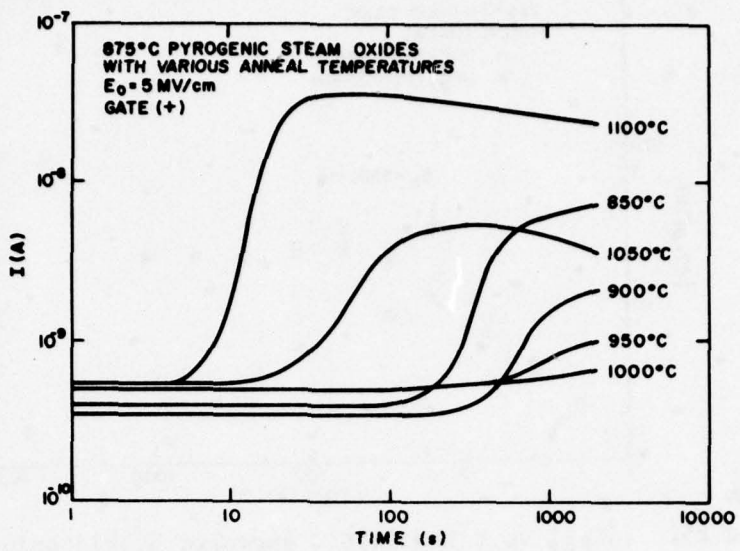


Figure 23. Time dependence of current during irradiation for pyrogenic steam oxides which were annealed at the temperatures shown. Positive gate bias of 5 MV/cm was used. Other conditions were the same as in figure 17.

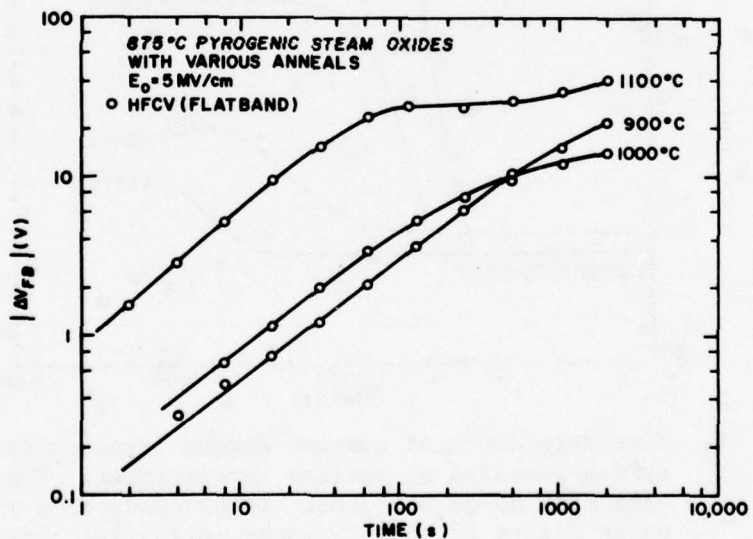


Figure 24. $|\Delta V_{FB}|$ vs t for various anneals of pyrogenic steam oxide. Positive gate bias of 5 MV/cm was used.

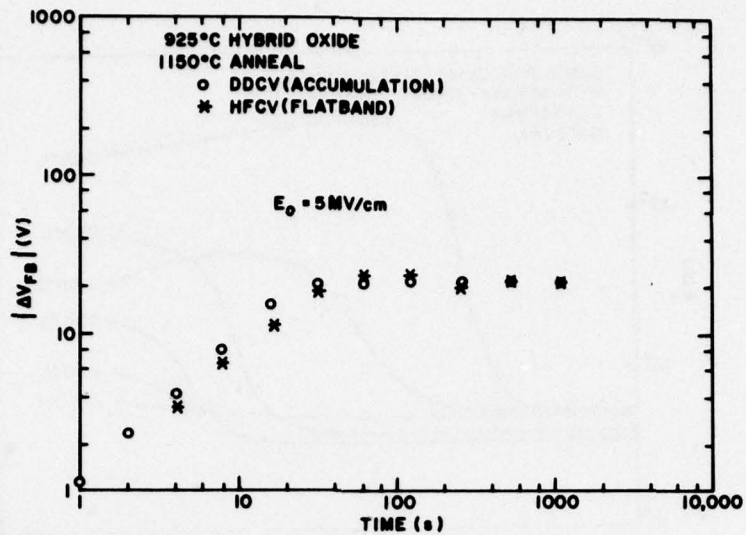


Figure 25. $|\Delta V_{FB}|$ vs t for 1150°C annealed hybrid oxide illustrating little interface state generation.

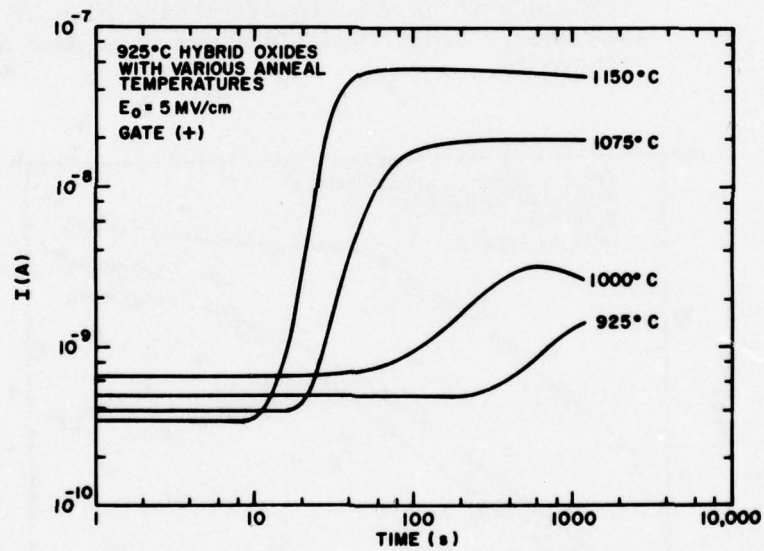


Figure 26. Time dependence of current during irradiation for hybrid oxides annealed at various temperatures. Positive gate bias of 5 MV/cm was used. Other conditions were the same as in figure 17. Differences in initial photocurrent due to varying thickness of semitransparent Al gate.

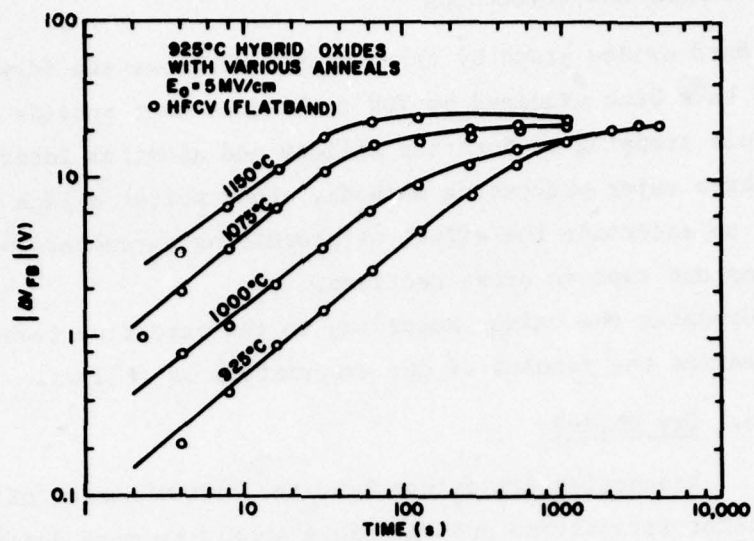


Figure 27. $|\Delta V_{FB}|$ vs t data for hybrid oxides annealed at various temperatures. Positive gate bias of 5 MV/cm was used.

5. SUMMARY AND CONCLUSION

Hard oxides grown by three different processes (dry, wet, and hybrid) have been examined by VUV techniques that provide information about hole trapping at both the silicon and aluminum interface. Within these three major processing methods, other softer oxides were also studied to ascertain the effect of processing parameters on hole-trap densities and capture cross sections.

Grouping the oxides according to the oxidation technique, we can summarize the results of our experiments as follows.

5.1 Dry Oxides

Unannealed dry oxides have the lowest number of interface states after irradiation and therefore should be more desirable for radiation applications where parameters such as switching speed are important. As a group these oxides are dominated by a hole trap with $S \sim 5 \times 10^{-14} \text{ cm}^2$ at 1 MV/cm. The DDCV measurements show no reversal in the ΔV_{FB} vs t data so that the few interface states seen after irradiation are probably donors.

Current-enhancement measurements were made on both annealed and unannealed oxides under positive and negative bias. The unannealed oxides show no enhancement reversal for any of the growth temperatures indicating few acceptor interface states. The 900° and 1000°C oxides are very hard with little current enhancement even at $E_o = 6 \text{ MV/cm}$. The enhancement under negative bias is actually larger than under positive bias for the 900° and 1000°C oxide which shows that more charge is trapped at the aluminum interface than at the silicon interface for these samples.

Annealing these oxides in argon substantially increases not only the number of hole traps near the silicon interface but also the number of acceptor interface states. The density of the hole traps near the aluminum interface is not affected much by the argon anneal.

5.2 Steam Oxide

Pyrogenic steam oxides have many more interface states than dry oxides even in hard samples. Many or all of these interface states are acceptors. As a group these oxides show $S \approx 5 \times 10^{-14} - 10^{-13}$ for $E_o = 1 \text{ MV/cm}$. The hardness of these oxides for high-energy irradiation ranges over an order of magnitude in ΔV_{FB} depending upon anneal temperature. Since all capture cross sections appear to be the same, the wide variation in ΔV_{FB} must be due to wide differences in hole trap and/or interface state densities. Current enhancement measurements show a very strong dependence on anneal temperature with 1000°C having the least enhancement and 850° and 1100°C the most. It is believed that the 900°C annealed oxide has the least number of hole traps and that the 1000°C oxide has less enhancement because of more acceptor interface states. The optimum anneal temperature for steam oxides is equal to or not much greater than the oxidation temperature.

5.3 Hybrid Oxides

In contrast to the other two processes, the hybrid oxides show $S \approx 2 \times 10^{-13} \text{ cm}^2$ (at $E_o = 1 \text{ MV/cm}$) up to 4 times larger than the wet or dry oxide capture cross sections. This is the only group of oxides grown with HCl present during oxidation. It is suspected that the HCl modifies the SiO_2 properties to the extent that the capture cross section is different. More than the other oxides the capture cross sections for the hybrid oxides overlap within the group. The main differences appear to be the hole trap and interface state density (of which many are acceptors).

The current-enhancement data for the hybrid oxides is similar to the wet oxide data. The enhancement increases with anneal temperature and has a minimum at the oxidation temperature. One anomaly among all the oxides is the 1150°C annealed hybrid oxide. It has a very large flatband voltage shift and current enhancement but very few interface states. All other hybrid oxides show substantial acceptor interface-state generation.

If we make the assumption that different hole traps have substantially different capture cross sections, then the wet and dry oxide data support the conclusion that the same trap is responsible for radiation charging in both oxides. This is somewhat surprising in view of the fact that the oxides are grown by completely different processes. However, it may be that the anneal of steam oxides in an inert ambient restructures the Si-SiO₂ interfacial region to be more like dry SiO₂.

The field dependence of the capture cross section was explained in section 4 as resulting from Poole-Frenkel type lowering of the short range potential barrier surrounding a neutral trap. This could have favorable implications for radiation hardening if devices are not irradiated to saturation. If MOS transistors are fabricated with thin oxides, then not only will the oxide field be larger for a given supply voltage, but the thickness dependence of ΔV_{FB} will make the device much harder.^{26,27}

Because of the various limitations of the measurement technique described in section 3 it is not possible to measure S and N_T with any greater accuracy using this method. Ning has shown how these parameters can be measured more accurately if one can measure both the injected charge and the flatband shift to a high degree of accuracy.²¹ Because of possible charge detrapping with changes in bias, it is not possible to measure ΔV_{FB} more accurately using MOS capacitors. Ning has used MOS transistors to measure threshold-voltage shifts very accurately, presumably because the oxide field is unchanged throughout the measurement.²¹ Unfortunately his technique relies on injected

²⁶ G. F. Derbenwick and B. L. Gregory, *IEEE Trans. Nucl. Sci.* NS-22, 2151 (1975).

²⁷ G. W. Hughes, R. J. Powell, and M. H. Woods, *Appl. Phys. Lett.* 29, 377 (1976).

charge from the silicon interface as the probe. This places a limitation on the maximum trapping efficiency that can be measured ($P_{co} \leq 0.1$). With VUV hole and electron excitation at the gate interface, this limitation is overcome since all charge arriving at the Si-SiO₂ interface is measured as a displacement current in the external circuit whether it is trapped or not. Using Ning's approach for measuring threshold-voltage shifts and exciting holes (or electrons) with 10.2-eV VUV photons, we should be able to measure S and N_T over a much wider range of cross sections and with much more accuracy than has been demonstrated at this time. This holds true for hole and electron capture cross sections.

REFERENCES

1. J. R. Srour, S. Othmer, O. L. Curtis, Jr., and K. Y. Chiu, IEEE Trans. Nucl. Sci. NS-23, 1513 (1976).
2. F. B. McLean, H. E. Boesch, Jr., and J. M. McGarrity, IEEE Trans. Nucl. Sci. NS-23, 1506 (1976) and H. E. Boesch, Jr., F. B. McLean, J. M. McGarrity, and G. A. Ausman, Jr., IEEE Trans. Nucl. Sci. NS-22, 2163 (1975).
3. R. C. Hughes, Bull. Am. Phys. Soc. 21, 404 (1976).
4. T. H. DiStephano and D. E. Eastman, Sol. State Comm. 9, 2259 (1971).
5. G. H. Sigel, Jr., E. J. Friebele, R. J. Ginther, and D. L. Griscom, IEEE Trans. Nucl. Sci. NS-21, 56 (1974).
6. C. T. Sah, IEEE Trans. Nucl. Sci. NS-23, 1563 (1976).
7. B. L. Gregory, IEEE Trans. Nucl. Sci. NS-22, 2295 (1975).
8. G. W. Hughes and R. J. Powell, IEEE Trans. Nucl. Sci. NS-23, 1569 (1976).
9. G. W. Hughes, "Radiation and Charge Transport in SiO₂," Final Report prepared under Contract N00014-74-C-0185 for Office of Naval Research, July 1977.
10. T. H. Ning and H. N. Yu, J. Appl. Phys. 45, 5373 (1974).
11. J. M. Aitken, D. J. DiMaria, and D. R. Young, IEEE Trans. Nucl. Sci. NS-23, 1526 (1976).
12. R. J. Powell, J. Appl. Phys. 46, 4557 (1975).
13. G. W. Hughes, J. Appl. Phys. 48, 5357 (1977).
14. R. J. Powell and G. W. Hughes, "Radiation and Charge Transport in SiO₂," Annual Report prepared under Contract N00014-74-C-0185 for Office of Naval Research, January 1975.
15. F. P. Heiman and G. Warfield, IEEE Trans. Electron. Devices ED-12, 167 (1965).
16. L. Katz and A. S. Penfold, Rev. of Modern Physics 24, 28 (1952).
17. J. R. Srour, O. L. Curtis, and K. Y. Chiu, IEEE Trans. Nucl. Sci. NS-21, 73 (1974). For analysis of data in preceding reference, see G. A. Ausman, Jr. and F. B. McLean, Appl. Phys. Letters 26, 173 (1975).
18. G. W. Hughes, R. M. Hughes, and R. M. White, IEEE Trans. Electron. Devices ED-22, 945 (1975).
19. J. G. Simmons and L. S. Wei, Solid State Electronics 16, 53 (1973).

20. S. M. Sze, *Physics of Semiconductor Devices* (John Wiley & Sons, New York, 1969), p. 455.
21. T. H. Ning, *J. Appl. Phys.* 47, 3203 (1976).
22. J. G. Simmons, *Phys. Rev.* 155, 657 (1967).
23. P. C. Arnett and N. Klein, *J. Appl. Phys.* 46, 1400 (1975).
24. A. K. Jonscher, *Thin Solid Film* 1, 213 (1967).
25. R. J. Powell, "Radiation and Charge Injection in Al_2O_3 using New Techniques" Final Report No. AFGL-TR-76-0017 for Air Force Geophysics Laboratory, January 1976.
26. G. F. Derbenwick and B. L. Gregory, *IEEE Trans. Nucl. Sci.* NS-22, 2151 (1975).
27. G. W. Hughes, R. J. Powell, and M. H. Woods, *Appl. Phys. Lett.* 29, 377 (1976).

APPENDIX

APPENDIX A. CALCULATION OF CAPTURE CROSS SECTION AND TRAP DENSITY

To calculate the capture cross section S and the trap density N_T for the various oxides, two different sets of data are needed. The initial flatband shift as a function of time is used to determine the product $N_T S$ through the use of equation (21) from the main body of this report. This assumes ΔV_{FB} is initially linear with t . This is true for most oxides, but there is one exception: the 925°C annealed hybrid oxide (see fig. A-1). Equation (21) was used for this case anyway, as a first approximation to $N_T S$. Figures A-1 through A-3 contain these data for all oxides measured at $E_0 = 1 \text{ MV/cm}$.

The final ΔV_{FB} was determined from the DDCV and HFCV data as explained in section 3 of this report. ΔV_{FBF} is not a strong function of applied field as long as E_0 is large enough to inhibit geminate recombination at the gate (see fig. 16 in the main body of the report). These measurements were only taken at $E_0 = 5 \text{ MV/cm}$. Fields of this magnitude as necessary to eliminate any reduction in hole generation rate due to charge build-up at the gate.^{A-1} Figures 11 and 25 and figures A-4 through A-11 contain these data for all oxides measured at $E_0 = 5 \text{ MV/cm}$.

^{A-1} R. J. Powell, *J. Appl. Phys.* 46, 4557 (1975).

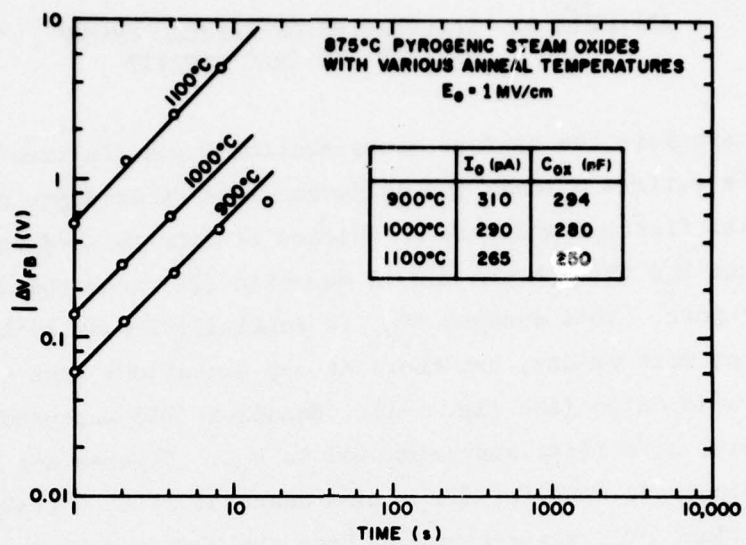


Figure A-1. $|\Delta V_{FB}|$ vs time "early" data for pyrogenic steam oxides annealed at various temperatures.

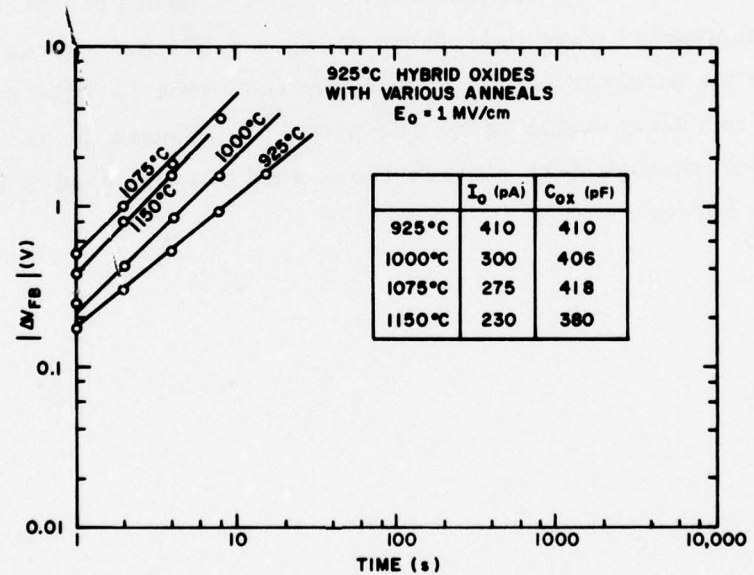


Figure A-2. $|\Delta V_{FB}|$ vs time "early" data for hybrid oxides annealed at various temperatures.

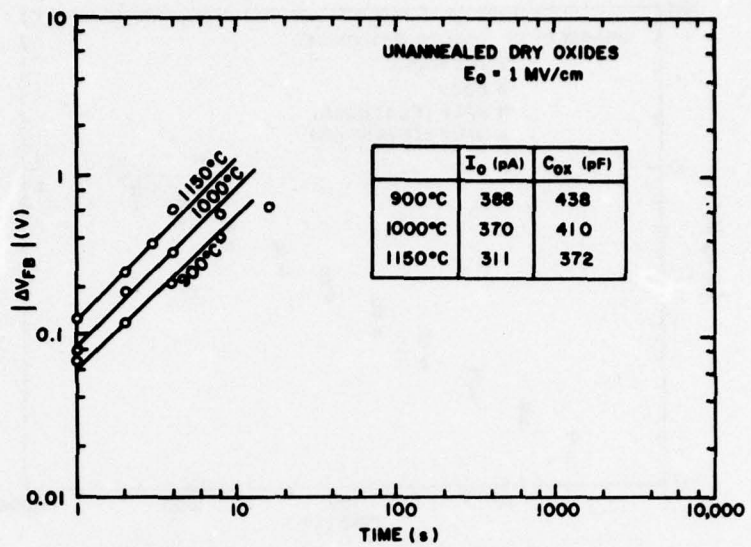


Figure A-3. $|\Delta V_{FB}|$ vs time "early" data for unannealed dry oxides grown at various temperatures.

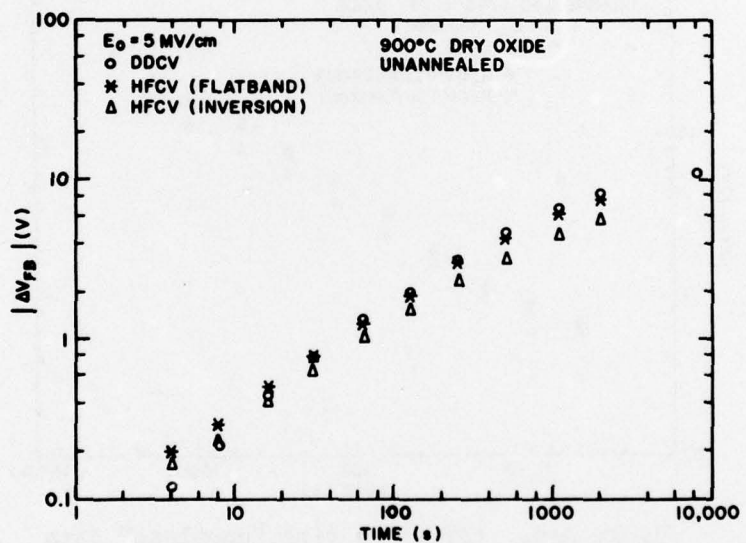


Figure A-4. $|\Delta V_{FB}|$ vs time "complete" data for 900°C dry oxides.

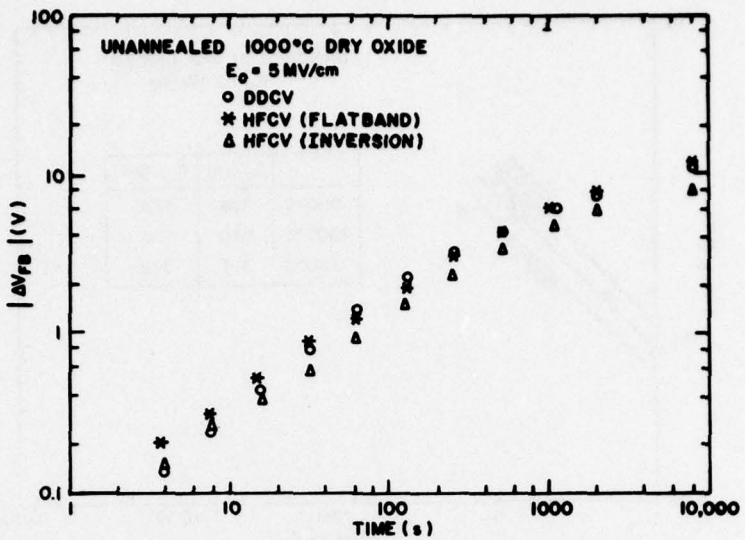


Figure A-5. $|\Delta V_{FB}|$ vs time "complete" data for 1000°C dry oxides.

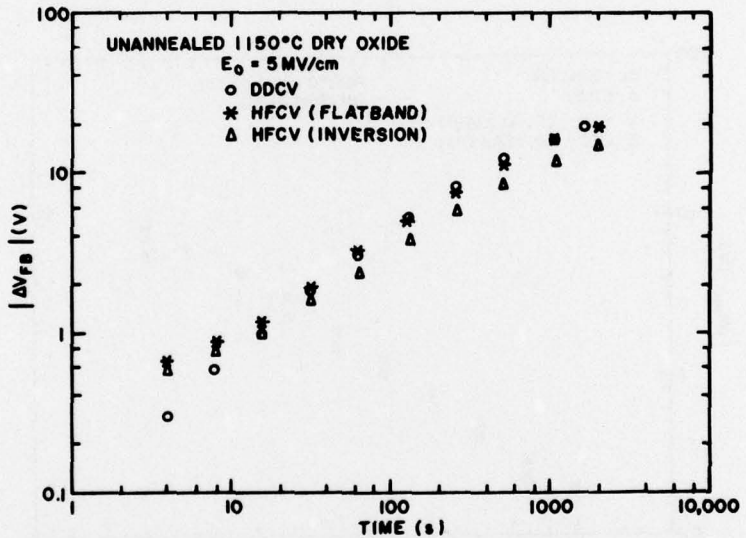


Figure A-6. $|\Delta V_{FB}|$ vs time "complete" data for 1150°C dry oxides.

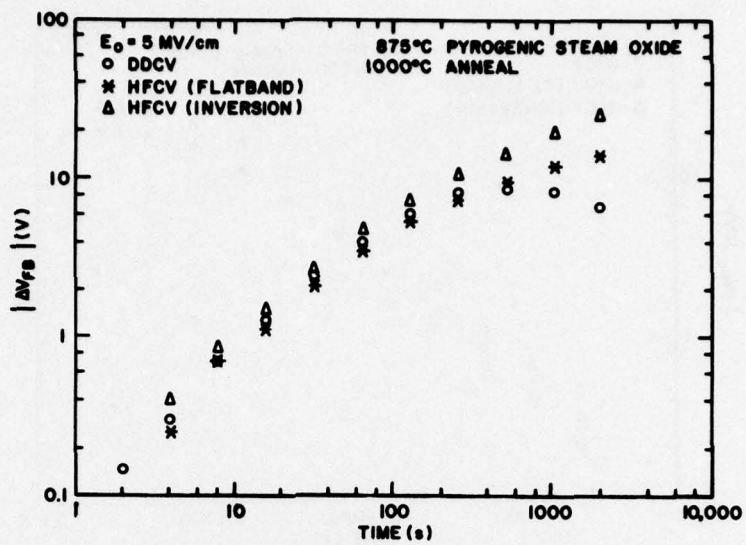


Figure A-7. $|\Delta V_{FB}|$ vs time "complete" data for 1000°C annealed pyrogenic steam oxide.

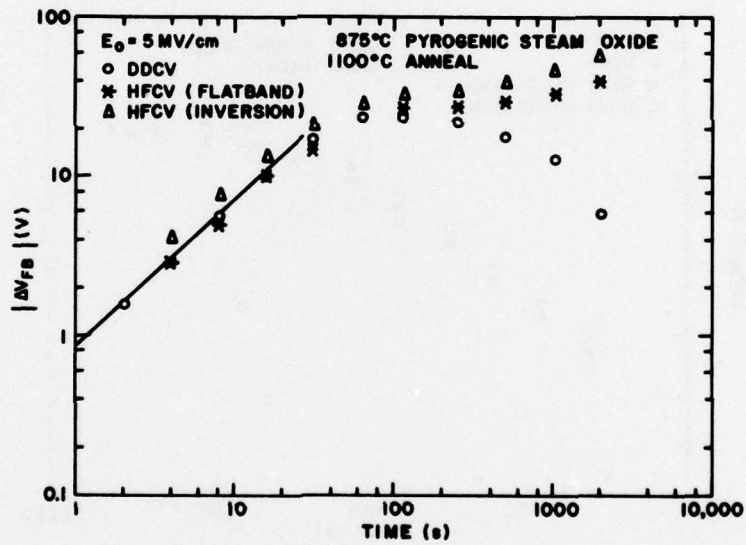


Figure A-8. $|\Delta V_{FB}|$ vs time "complete" data for 1100°C annealed pyrogenic steam oxide.

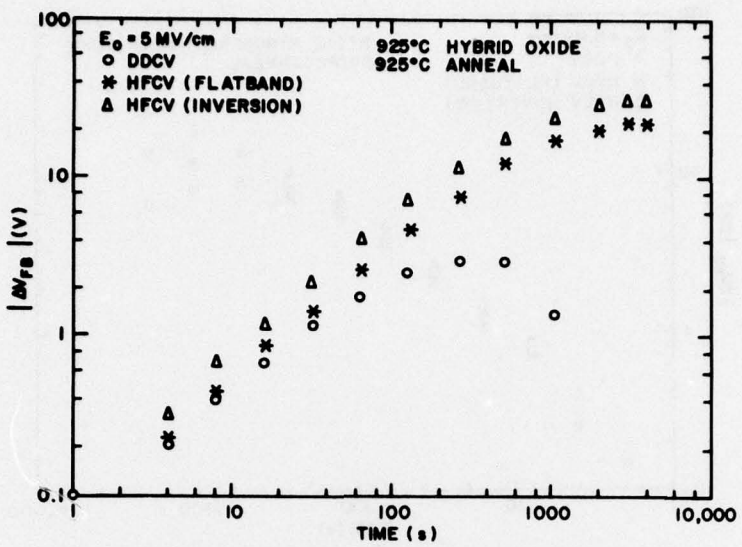


Figure A-9. $|\Delta V_{FB}|$ vs time "complete" data for 925°C annealed hybrid oxide.

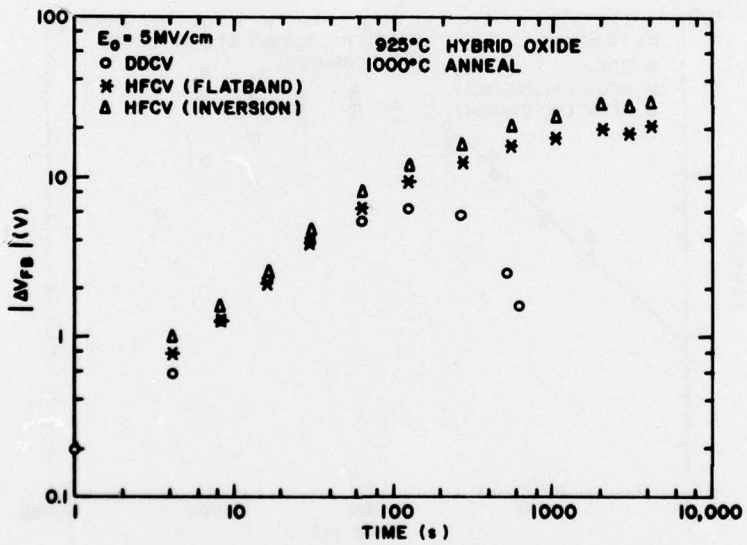


Figure A-10. $|\Delta V_{FB}|$ vs time "complete" data for 1000°C annealed hybrid oxide.

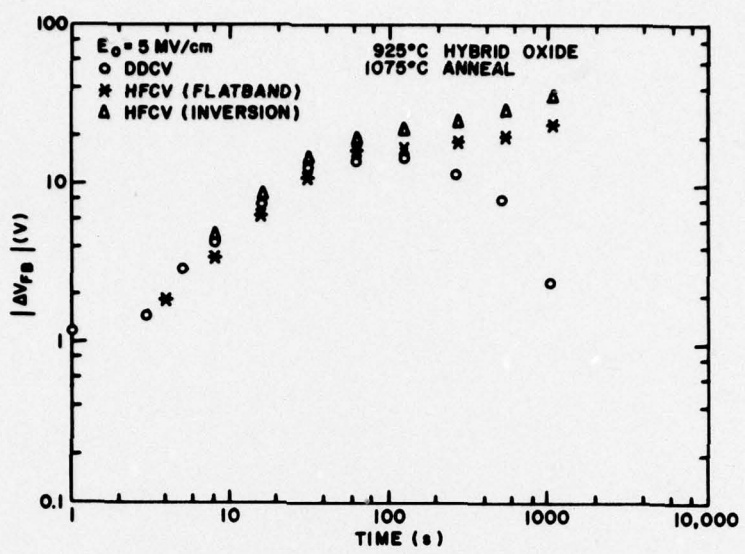


Figure A-11. $|\Delta V_{FB}|$ vs time "complete" data for 1075°C annealed hybrid oxide.

DISTRIBUTION LIST

<p>Director Defense Communications Agency Washington, DC 20305 Attn: Code 930, M.I. Burgett</p> <p>Defense Documentation Center Cameron Station Alexandria, VA 22314 (12)</p> <p>Director Defense Intelligence Agency Washington, DC 20301 Attn: DS-4A2</p> <p>Director Defense Nuclear Agency Washington, DC 20305 Attn: DDST</p> <p>Director Defense Nuclear Agency Washington, DC 20305 Attn: TITL Tech Library (3)</p> <p>Director Defense Nuclear Agency Washington, DC 20305 Attn: RAEV</p> <p>Director Defense Nuclear Agency Washington, DC 20305 Attn: RATN</p> <p>Director Defense Nuclear Agency Washington, DC 20305 Attn: STVL</p> <p>Dir of Defense Rsch & Eng Department of Defense Washington, DC 20301 Attn: S&SS (OS)</p> <p>Commander Field Command Defense Nuclear Agency Kirtland AFB, NM 87115 Attn: FCPR</p> <p>Director Interservice Nuclear Weapons Sch Kirtland AFB, NM 87115 Attn: Document Control</p>	<p>Director Joint Strat Tgt Planning Staff JCS - JLTW-2 Offutt AFB Omaha, NB 68113</p> <p>Livermore Div Fld Command DNA Livermore Laboratory P.O. Box 808 Livermore, CA 94550 Attn: FCPR</p> <p>Director National Security Agency Ft. George G. Meade, MD 20755 Attn: O.O. Van Gunten, R-425</p> <p>Director National Security Agency Ft. George G. Meade, MD 20755 Attn: TDL</p> <p>Project Manager Army Tactical Data Systems U.S. Army Electronics Command Fort Monmouth, NJ 07703 Attn: D.B. Huewe</p> <p>Project Manager Army Tactical Data Systems U.S. Army Electronics Command Fort Monmouth, NJ 07703 Attn: DRCPN-TDS-SD</p> <p>Commander BMD System Command P.O. Box 1500 Huntsville, AL 35807 Attn: BDMSC-TEN</p> <p>Commander Frankford Arsenal Bridge & Tacony Sts Philadelphia, PA 19137 Attn: SARFA-FCD</p> <p>Commander Harry Diamond Laboratories 2800 Powder Mill Road Adelphi, MD 20783 Attn: J. Halpin</p> <p>Commander Harry Diamond Laboratories 2800 Powder Mill Road Adelphi, MD 20783 Attn: DRSCO-TI, Tech Lib (3)</p> <p>Commander Harry Diamond Laboratories 2800 Powder Mill Road Adelphi, MD 20783 Attn: DRXDO-RCC</p>	<p>Commander Harry Diamond Laboratories 2800 Powder Mill Road Adelphi, MD 20783 Attn: DRXDO-NP</p> <p>Commander Harry Diamond Laboratories 2800 Powder Mill Road Adelphi, MD 20783 Attn: DRXDO-RCC</p> <p>Commander Harry Diamond Laboratories 2800 Powder Mill Road Adelphi, MD 20783 Attn: J. McGarrity</p> <p>Commander Harry Diamond Laboratories 2800 Powder Mill Road Adelphi, MD 20783 Attn: DRXDO-RC</p> <p>Commander Harry Diamond Laboratories 2800 Powder Mill Road Adelphi, MD 20783 Attn: DRXDO-EM</p> <p>Commander Harry Diamond Laboratories 2800 Powder Mill Road Adelphi, MD 20783 Attn: DRXDO-RBH</p> <p>Commander Harry Diamond Laboratories 2800 Powder Mill Road Adelphi, MD 20783 Attn: DRXDO-AS</p> <p>Commander Harry Diamond Laboratories 2800 Powder Mill Road Adelphi, MD 20783 Attn: Chairman, Editorial Cmte</p> <p>Commander Harry Diamond Laboratories 2800 Powder Mill Road Adelphi, MD 20783 Attn: DRXDO-RBH, F. McLean (10)</p> <p>Commander Harry Diamond Laboratories 2800 Powder Mill Road Adelphi, MD 20783 Attn: DRXDO-TI, Tech Reports</p> <p>Commander Harry Diamond Laboratories 2800 Powder Mill Road Adelphi, MD 20783 Attn: DRXDO-RD, Q.C. Kaiser</p>
---	---	--

Commander Picatinny Arsenal Dover, NJ 07801 Attn: SMUPA-ND-W	Chief U.S. Army Communications Sys Agency Fort Monmouth, NJ 07703 Attn: SCCM-AD-SV, Library	Commander U.S. Army Missile Command Redstone Arsenal, AL 35809 Attn: DRCPM-LCEX
Commander Picatinny Arsenal Dover, NJ 07801 Attn: SMUPA-ND-N-E	Commander U.S. Army Electronics Command Fort Monmouth, NJ 07703 Attn: DRSEL-TL-MD	Commander U.S. Army Missile Command Redstone Arsenal, AL 35809 Attn: DRSMI-RGP
Commander Picatinny Arsenal Dover, NJ 07801 Attn: SARPA-ND-C-E	Commander U.S. Army Electronics Command Fort Monmouth, NJ 07703 Attn: DRSEL-TL-EN	Commander U.S. Army Missile Command Redstone Arsenal, AL 35809 Attn: DRSMI-RRR
Commander Picatinny Arsenal Dover, NJ 07801 Attn: SARPA-FR-F	Commander U.S. Army Electronics Command Fort Monmouth, NJ 07703 Attn: DRSEL-CT-HDK	Commander U.S. Army Missile Command Redstone Arsenal, AL 35809 Attn: DRCPM-PE-EA
Commander Picatinny Arsenal Dover, NJ 07801 Attn: SARPA-ND-N	Commander U.S. Army Electronics Command Fort Monmouth, NJ 07703 Attn: DRSEL-GG-TD	Commander U.S. Army Mobility Equip R&D Ctr Fort Belvoir, VA 22060 Attn: STSFB-MM
Commander Redstone Scientific Info Ctr U.S. Army Missile Command Redstone Arsenal, AL 35809 Attn: Chief, Documents (3)	Commander U.S. Army Electronics Command Fort Monmouth, NJ 07703 Attn: DRSEL-TL-IR	Chief U.S. Army Nuc & Chemical Surety Bldg 2073, North Area Ft. Belvoir, VA 22060 Attn: MOSG-ND
Secretary of the Army Washington, DC 20310 Attn: ODUSA-OR	Commander U.S. Army Electronics Command Fort Monmouth, NJ 07703 Attn: DRSEL-TL-ND	Commander U.S. Army Nuclear Agency 7500 Backlick Rd, Bldg 2073 Springfield, VA 22150 Attn: ATCN-W
Director TRASANA White Sands Missile Range New Mexico 88002 Attn: ATAA-EAC	Commander U.S. Army Electronics Command Fort Monmouth, NJ 07703 Attn: DRSEL-TL-EN	Commander U.S. Army Test & Eval Command Aberdeen Prvng Ground, MD 21005 Attn: DRSTE-EL
Director U.S. Army Ballistic Research Lbs Aberdeen Prvng Ground, MD 21005 Attn: DRXBR-AM	Commander U.S. Army Electronics Command Fort Monmouth, NJ 07703 Attn: DRSEL-PL-ENV	Commander U.S. Army Test & Eval Command Aberdeen Prvng Ground, MD 21005 Attn: DRSTE-NB
Director U.S. Army Ballistic Research Lbs Aberdeen Prvng Ground, MD 21005 Attn: DRXBR-X	Commander-In-Chief U.S. Army Europe & Seventh Army APO New York 09403 Attn: ODCSE-E AEAGE-PI	Chief of Naval Research Navy Department Arlington, VA 22217 Attn: Code 421
Director U.S. Army Ballistic Research Lbs Aberdeen Prvng Ground, MD 21005 Attn: DRXRD-BVL	Commander U.S. Army Missile Command Redstone Arsenal, AL 35809 Attn: DRSMI-RGD	Chief of Naval Research Navy Department Arlington, VA 22217 Attn: Code 427

Commander Naval Electronic Sys Command Washington, DC 20360 Attn: PME 117-21	Commander Naval Research Laboratory Washington, DC 20375 Attn: Code 5210	Commanding Officer Nuclear Weapons Tng Ctr Pacific Naval Air Station, North Island San Diego, CA 92135 Attn: Code 50
Commander Naval Electronic Sys Command Washington, DC 20360 Attn: Code 504510	Commander Naval Sea Systems Command Navy Department Washington, DC 20362 Attn: SEA-9931	Director Strategic Sys Project Office Navy Department Washington, DC 20376 Attn: NSP-2342
Commander Naval Electronic Sys Command Washington, DC 20360 Attn: ELEX 05323	Commander Naval Sea Systems Command Navy Department Washington, DC 20362 Attn: SEA-9931	AF Geophysics Laboratory, AFSC Hanscom AFB, MA 01731 Attn: J.E. Cormier
Commanding Officer Naval Intelligence Support Ctr 4301 Suitland Road, Bldg 5 Washington, DC 20390 Attn: P. Alexander	Commander Naval Ship Engineering Ctr Washington, DC 20362 Attn: Code 6174D2	AF Geophysics Laboratory, AFSC Hanscom AFB, MA 01731 Attn: LOR, E.A. Burke
Director Naval Research Laboratory Washington, DC 20375 Attn: Code 6631	Officer-In-Charge Naval Surface Weapons Center White Oak Silver Spring, MD 20910 Attn: Code WA52	AF Institute of Technology, AU Wright-Patterson AFB, OH 45433 Attn: ENP, C.J. Bridgman
Director Naval Research Laboratory Washington, DC 20375 Attn: Code 5216	Officer-In-Charge Naval Surface Weapons Center White Oak Silver Spring, MD 20910 Attn: Code WA50	AF Materials Laboratory, AFSC Wright-Patterson AFB, OH 45433 Attn: LTE
Director Naval Research Laboratory Washington, DC 20375 Attn: Code 7701	Officer-In-Charge Naval Surface Weapons Center White Oak Silver Spring, MD 20910 Attn: Code WA501, NNPO	AF Weapons Laboratory, AFSC Kirtland AFB, NM 87117 Attn: ELS
Director Naval Research Laboratory Washington, DC 20375 Attn: Code 6440	Commander Naval Surface Weapons Center Dahlgren Laboratory Dahlgren, VA 22448 Attn: W.H. Holt	AF Weapons Laboratory, AFSC Kirtland AFB, NM 87117 Attn: ELA
Director Naval Research Laboratory Washington, DC 20375 Attn: Code 601	Commander Naval Weapons Center China Lake, CA 93555 Attn: Code 533, Tech Lib	AF Weapons Laboratory, AFSC Kirtland AFB, NM 87117 Attn: DES
Director Naval Research Laboratory Washington, DC 20375 Attn: Code 2627	Commanding Officer Naval Weapons Support Center Crane, IN 47522 Attn: Code 7024	AF Weapons Laboratory, AFSC Kirtland AFB, NM 87117 Attn: NTS
Director Naval Research Laboratory Washington, DC 20375 Attn: Code 4004	Commanding Officer Naval Weapons Support Center Crane, IN 47522 Attn: Code 70242	AF Weapons Laboratory, AFSC Kirtland AFB, NM 87117 Attn: ELP

AF Weapons Laboratory, AFSC Kirtland AFB, NM 87117 Attn: SAB	Commander Rome Air Development Ctr, AFSC Hanscom AFB, MA 01731 Attn: ET, R. Buchanan	University of California Livermore Laboratory P.O. Box 808 Livermore, CA 94550 Attn: Tech Info Dept L-3
AFTAC Patrick AFB, FL 32925 Attn: TAE	SAMSO P.O. Box 92960 Worldway Postal Center Los Angeles, CA 90009 Attn: DYS	University of California Livermore Laboratory P.O. Box 808 Livermore, CA 94550 Attn: R.L. Ott L-531
AFTAC Patrick AFB, FL 32925 Attn: TFS	SAMSO P.O. Box 92960 Worldway Postal Center Los Angeles, CA 90009 Attn: YEE	University of California Livermore Laboratory P.O. Box 808 Livermore, CA 94550 Attn: J.E. Keller L-125
Air Force Avionics Lab, AFSC Wright-Patterson AFB, OH 45433 Attn: AAT, M. Friar	SAMSO/IN P.O. Box 92960 Worldway Postal Center Los Angeles, CA 90009 Attn: IND I J Judy	University of California Livermore Laboratory P.O. Box 808 Livermore, CA 94550 Attn: H. Kruger L-96
Air Force Avionics Lab, AFSC Wright-Patterson AFB, OH 45433 Attn: DH, LTC McKenzie	SAMSO/MN Norton AFB, CA 92409 Attn: MNHH	University of California Livermore Labojratory P.O. Box 808 Livermore, CA 94550 Attn: L. Cleland L-156
Air Force Avionics Lab, AFSC Wright-Patterson AFB, OH 45433 Attn: DHE, H.J. Hennecke	SAMSO/MN Norton AFB, CA 92409 Attn: MNNG	University of California Livermore Laboratory P.O. Box 808 Livermore, CA 94550 Attn: F. Kovar L-31
Commander ASD Wright-Patterson AFB, OH 45433 Attn: ENACC, R.L. Fish	SAMSO/RS P.O. Box 92960 Worldway Postal Center Los Angeles, CA 90009 Attn: RSSE	University of California Livermore Laboratory P.O. Box 808 Livermore, CA 94550 Attn: D. Meeker L-545
Headquarters Electronic Systems Div/YS Hanscom AFB, MA 01731 Attn: YSEV	SAMSO/RS P.O. Box 92960 Worldway Postal Center Los Angeles, CA 90009 Attn: RSMG	Los Alamos Scientific Lab P.O. Box 1663 Los Alamos, NM 87545 Attn: Doc Con for B.W. Noel
Commander Foreign Technology Div, AFSC Wright-Patterson AFB, OH 45433 Attn: ETDP	SAMSO/SZ P.O. Box 92960 Worldway Postal Center Los Angeles, CA 90009 Attn: SZJ	Los Alamos Scientific Lab P.O. Box 1663 Los Alamos, NM 87545 Attn: Doc Con for J.A. Freed
Commander Rome Air Development Ctr, AFSC Griffiss AFB, NY 13440 Attn: RBRP	Commander-In-Chief Strategic Air Command Offutt AFB, NB 68113 Attn: NRI-STINFO Library	Los Alamos Scientific Lab P.O. Box 1663 Los Alamos, NM 87545 Attn: Doc for M.W. Hoffman
Commander Rome Air Development Ctr, AFSC Hanscom AFB, MA 01731 Attn: ETS, R. Dolan	Commander-In-Chief Strategic Air Command Offutt AFB, NB 68113 Attn: XPFS	Sandia Laboratories Livermore Laboratory P.O. Box 969 Livermore, CA 94550 Attn: Doc Con for T.A. Dillin

Control Data Corporation P.O. Box 0 Minneapolis, MN 55440 Attn: J. Meehan	Ford Aerospace & Comm Corp 3939 Fabian Way Palo Alto, CA 94303 Attn: D.R. McMorrow, MS G30	General Electric Tempo-Center for Adv Studies 816 State Street Santa Barbara, CA 93102 Attn: R.R. Rutherford
Cutler-Hammer, Inc AIL Division Comac Road Deer Park, NY 11729 Attn: Central Tech Files	Ford Aerospace & Comm Operations Ford & Jamboree Roads Newport Beach, CA 92663 Attn: Tech Info Section	General Electric Tempo-Center for Adv Studies 816 State Street Santa Barbara, CA 93102 Attn: DASIAAC
Dikewood Industries, Inc 1009 Bradbury Drive, S.E. Albuquerque, NM 87106 Attn: L. Wayne Davis	Ford Aerospace & Comm Operations Ford & Jamboree Roads Newport Beach, CA 92663 Attn: K.C. Attinger	General Electric Tempo-Center for Adv Studies 816 State Street Santa Barbara, CA 93102 Attn: M. Fspig
E-Systems, Inc Greenville Division P.O. Box 1056 Greenville, TX 75401 Attn: Library 8-50100	Franklin Institute 20th Street & Parkway Philadelphia, PA 19103 Attn: R.H. Thompson	General Electric Aircraft Eng Bus Group Evendale Plant Int Hwy 755 Cincinnati, OH 45215 Attn: J.A. Ellerhorst E2
Effects Technology, Inc 5383 Hollister Avenue Santa Barbara, CA 93111 Attn: E.J. Steele	General Dynamics Corp Electronics Div P.O. Box 2566 Orlando, FL 32802 Attn: D.W. Coleman	General Electric Aerospace Electronics Systems French Road Utica, NY 13503 Attn: W.J. Patterson Drop 233
Exp & Math Physics Consultants P.O. Box 66331 Los Angeles, CA 90066 Attn: T.M. Jordan	General Electric Valley Forge Space Center P.O. Box 8555 Philadelphia, PA 19101 Attn: J.C. Peden RM 4230M	General Electric P.O. Box 5000 Binghamton, NY 13902 Attn: D.W. Pepin Drop 160
Fairchild Camera & Instrument 464 Ellis Street Mountain View, CA 94040 Attn: Sec Dept for 2-233 D.K. Myers	General Electric Valley Forge Space Center P.O. Box 8555 Philadelphia, PA 19101 Attn: J.L. Andrews	General Electric Attn: DASIAAC c/o Defense Nuclear Agency Washington, DC 20305 Attn: W. Alfonte
Fairchild Industries, Inc Fairchild Technology Center 20301 Century Boulevard Germantown, MD 20767 Attn: Mgr, Config Data & Stdrds	General Electric Valley Forge Space Center P.O. Box 8555 Philadelphia, PA 19101 Attn: L.I. Chasen	General Research Corp P.O. Box 3587 Santa Barbara, CA 93105 Attn: R.D. Hill
University of Florida P.O. Box 284 Gainesville, FL 32601 Attn: P.B. Rambo	General Electric Re-Entry & Environmental Sys Div P.O. Box 7722 Philadelphia, PA 19101 Attn: R.V. Benedict	Georgia Institute of Tech Georgia Tech Research Inst Atlanta, GA 30332 Attn: R. Curry
University of Florida P.O. Box 284 Gainesville, FL 32601 Attn: D.P. Kennedy	General Electric Re-Entry & Environmental Sys Div P.O. Box 7722 Philadelphia, PA 19101 Attn: J.W. Palchefskey Jr	Grumman Aerospace Corp South Oyster Bay Road Bethpage, NY 11714 Attn: J. Rogers Dept 533
Ford Aerospace & Comm Corp 3939 Fabian Way Palo Alto, CA 94303 Attn: S.R. Crawford, MS 531	General Electric Ordnance Systems 100 Plastics Avenue Pittsfield, MA 01201 Attn: J.J. Reidl	GTE Sylvania, Inc Electronics Systems Grp 77 A Street Needham, MA 02194 Attn: L.L. Blaisdell

Sandia Laboratories P.O. Box 5800 Albuquerque, NM 87115 Attn: Doc Con for ORG 2110 J.A. Hood	Aerospace Corporation P.O. Box 92957 Los Angeles, CA 90009 Attn: W.W. Willis	Boeing Company P.O. Box 3707 Seattle, WA 98124 Attn: C. Rosenberg 2R-00
Sandia Laboratories P.O. Box 5800 Albuquerque, NM 87115 Attn: Doc Con for 3141 Sandia Rpt Col	Aerospace Corporation P.O. Box 92957 Los Angeles, CA 90009 Attn: I.M. Garfunkel	Boeing Company P.O. Box 3707 Seattle, WA 98124 Attn: I. Amura 2R-00
Sandia Laboratories P.O. Box 5800 Albuquerque, NM 87115 Attn: Div 5231, J.H. Renken	Aerospace Corporation P.O. Box 92957 Los Angeles, CA 90009 Attn: L.W. Aukerman	Boeing Company P.O. Box 3707 Seattle, WA 98124 Attn: H.W. Wicklein MS 17-11
Sandia Laboratories P.O. Box 5800 Albuquerque, NM 87115 Attn: Doc Con for ORG 1933 F. Coppage	Aerospace Corporation P.O. Box 92957 Los Angeles, CA 90009 Attn: Library	Boeing Company P.O. Box 3707 Seattle, WA 98124 Attn: R.S. Caldwell 2R-00
Sandia Laboratories P.O. Box 5800 Albuquerque, NM 87115 Attn: Doc Con for ORG 2140 R. Gregory	Aerospace Corporation P.O. Box 92957 Los Angeles, CA 90009 Attn: J. Reinheimer	Booz-Allen & Hamilton, Inc 106 Apple Street Tinton Falls, NJ 07724 Attn: R.J. Chrisner
Sandia Laboratories P.O. Box 5800 Albuquerque, NM 87115 Attn: Doc Con for J.V. Walker	Avco Research & Systems Grp 201 Lowell Street Wilmington, MA 01887 Attn: Res Lib A830 RM 7201	California Institute of Tech Jet Propulsion Laboratory 4800 Oak Grove Drive Pasadena, CA 91103 Attn: J. Bryden
U.S. Department of Energy Albuquerque Operations Office P.O. Box 5400 Albuquerque, NM 87115 Attn: Doc Con for WSSB	BDM Corporation 7915 Jones Branch Drive McLean, VA 22701 Attn: T.H. Neighbors	California Institute of Tech Jet Propulsion Laboratory 4800 Oak Grove Drive Pasadena, CA 91103 Attn: A.G. Stanley
Central Intelligence Agency Attn: RD/SI RM 5G48 HQ Bldg Washington, DC 20505 Attn: A.A. Padgett	BDM Corporation P.O. Box 9274 Albuquerque International Albuquerque, NM 87119 Attn: D.R. Alexander	Charles Stark Draper Lab 555 Technology Square Cambridge, MA 02139 Attn: R.G. Haltmaier
Department of Commerce National Bureau of Standards Washington, DC 20234 Attn: Sec Officer for Appl Rad Div, R.C. Placious	Bendix Corporation Communication Division East Joppa Road Baltimore, MD 21204 Attn: Document Control	Charles Stark Draper Lab 555 Technology Square Cambridge, MA 02139 Attn: P.R. Kelly
Department of Commerce National Bureau of Standards Washington, DC 20234 Attn: Sec Officer for J.C. French	Bendix Corporation Research Laboratories Div Bendix Center Southfield, MI 48075 Attn: D.J. Niehaus	Charles Stark Draper Lab 555 Technology Square Cambridge, MA 02139 Attn: K. Fertig
Aerojet Electro-Systems Co Div of Aerojet-General Corp P.O. Box 296 Azusa, CA 91702 Attn: T.D. Hanscome	Boeing Company P.O. Box 3707 Seattle, WA 98124 Attn: Aerospace Library	Computer Sciences Corp 201 La Veta Drive N.E. Albuquerque, NM 87108 Attn: R.H. Dickhaut

GTE Sylvania, Inc Electronics Systems Grp 77 A Street Needham, MA 02194 Attn: C.A. Thornhill	Honeywell, Inc Avionics Division 13350 U.S. Highway 19 North St. Petersburg, FL 33733 Attn: S.H. Graff MS 725-J	IRT Corp P.O. Box 81087 San Diego, CA 92138 Attn: MDC
GTE Sylvania, Inc Electronics Systems Grp 77 A Street Needham, MA 02194 Attn: J.A. Waldon	Honeywell, Inc Radiation Center 2 Forbes Road Lexington, MA 02173 Attn: Tech Library	IRT Corp P.O. Box 81087 San Diego, CA 92138 Attn: J.A. Naber
GTE Sylvania, Inc 189 B Street Needham Heights, MA 02194 Attn: C.H. Ramsbottom	Hughes Aircraft Centinela & Teale Culver City, CA 90230 Attn: B.W. Campbell MS 6-E-110	Jaycor 205 S Whiting St, Suite 500 Alexandria, VA 22304 Attn: C. Turesko
GTE Sylvania, Inc 189 B Street Needham Heights, MA 02194 Attn: H.A. Ullman	Hughes Aircraft Centinela & Teale Culver City, CA 90230 Attn: K.R. Walker MS D157	Jaycor 205 S Whiting St, Suite 500 Alexandria, VA 22304 Attn: R. Sullivan
GTE Sylvania, Inc 189 B Street Needham Heights, MA 02194 Attn: P.B. Fredrickson	Hughes Aircraft Centinela & Teale Culver City, CA 90230 Attn: D. Binder MS 6-D147	Kaman Sciences Corp P.O. Box 7463 Colorado Springs, CO 80933 Attn: A.P. Bridges
GTE Sylvania, Inc 189 B Street Needham Heights, MA 02194 Attn: H&V Group	Hughes Aircraft P.O. Box 92919 El Segundo Site Los Angeles, CA 90009 Attn: E.C. Smith MS A620	Kaman Sciences Corp P.O. Box 7463 Colorado Springs, CO 80933 Attn: J.I. Lubell
Harris Corporation Harris Semiconductor Div P.O. Box 883 Melbourne, FL 32901 Attn: C.F. Davis MS 17-220	Hughes Aircraft P.O. Box 92919 El Segundo Site Los Angeles, CA 90009 Attn: W.W. Scott MS A1080	Kaman Sciences Corp P.O. Box 7463 Colorado Springs, CO 80933 Attn: D.H. Bryce
Harris Corporation Harris Semiconductor Div P.O. Box 883 Melbourne, FL 32901 Attn: T.L. Clark MS 4040	IBM Corp Route 17C Owego, NY 13827 Attn: F. Frankovsky	Kaman Sciences Corp P.O. Box 7463 Colorado Springs, CO 80933 Attn: W.E. Ware
Harris Corporation Harris Semiconductor Div P.O. Box 883 Melbourne, FL 32901 Attn: W.E. Abare MS 16-111	Ion Physics Corp South Bedford Street Burlington, MA 01803 Attn: R.D. Evans	Litton Systems, Inc Guidance & Cont Sys Div 5500 Canoga Ave Woodland Hills, CA 91364 Attn: V.J. Ashby MS 67
Hazeltine Corp Puleski Road Greenlawn, NY 11740 Attn: M. Waite	IRT Corp P.O. Box 81087 San Diego, CA 92138 Attn: R.L. Mertz	Litton Systems, Inc Guidance & Cont Sys Div 5500 Canoga Ave Woodland Hills, CA 91364 Attn: J.P. Retzler
Honeywell, Inc Avionics Division 2600 Ridgeway Parkway Minneapolis, MN 55413 Attn: R.R. Johnson A1622	IRT Corp P.O. Box 81087 San Diego, CA 92138 Attn: R.H. Stahl	Lockheed Missiles & Space P.O. Box 504 Sunnyvale, CA 94088 Attn: L. Rossi Dept 81-64

Lockheed Missiles & Space P.O. Box 504 Sunnyvale, CA 94088 Attn: B.T. Kimura Dept 81-14	Martin Marietta Corp P.O. Box 179 Denver, CO 80201 Attn: J.E. Goodwin MS 0452	Northrop Corp Research & Technology Center 3401 West Broadway Hawthorne, CA 90250 Attn: D.N. Pocock
Lockheed Missiles & Space P.O. Box 504 Sunnyvale, CA 94088 Attn: E.A. Smith Dept 85-85	McDonnell Douglas Corp P.O. Box 516 St. Louis, MO 63166 Attn: Tech Library	Northrop Corp Research & Technology Center 3401 West Broadway Hawthorne, CA 90250 Attn: J.R. Srour
Lockheed Missiles & Space P.O. Box 504 Sunnyvale, CA 94088 Attn: P.J. Hart Dept 81-14	McDonnell Douglas Corp 5301 Bolsa Ave Huntington Beach, CA 92647 Attn: S. Schneider	Northrop Corp Electronic Division 2301 West 120th Street Hawthorne, CA 92050 Attn: V.R. DeMartino
Lockheed Missiles & Space P.O. Box 504 Sunnyvale, CA 94088 Attn: P.J. Hart Dept 81-14	Mission Research Corp 735 State Street Santa Barbara, CA 93101 Attn: W.C. Hart	Physics International 2700 Merced Street San Leandro, CA 94577 Attn: Doc Con for C.H. Stallings
Lockheed Missiles & Space P.O. Box 504 Sunnyvale, CA 94088 Attn: S.I. Taimuty Dept 85-85	Mission Research Corp P.O. Box 1209 La Jolla, CA 92038 Attn: J.P. Raymond	Physics International 2700 Merced Street San Leandro, CA 94577 Attn: Doc Con for J.H. Huntington
Lockheed Missiles & Space 3251 Hanover Street Palo Alto, CA 94304 Attn: Tech Info Ctr D/Coll	Mission Research Corp P.O. Box 1209 La Jolla, CA 92038 Attn: V.A.J. Van Lint	R&D Associates P.O. Box 9695 Marina Del Rey, CA 90291 Attn: S.C. Rogers
MIT Lincoln Laboratory P.O. Box 73 Lexington, MA 02173 Attn: L. Loughlin A-082	National Academy of Sciences National Mat'l's Advisory Board 2101 Constitution Ave, NW Washington, DC 20418 Attn: R.S. Shane	Raytheon Company Hartwell Road Bedford, MA 01730 Attn: G.H. Joshi, Radar Sys Lab
Martin Marietta Aerospace P.O. Box 5837 Orlando, FL 32805 Attn: W.W. Mras MP-413	University of New Mexico 1821 Roma N.E. Albuquerque, NM 87106 Attn: W.W. Grannemann	RCA Astro Electronics P.O. Box 800 Princeton, NJ 08540 Attn: G.J. Brucker
Martin Marietta Aerospace P.O. Box 5837 Orlando, FL 32805 Attn: M.C. Griffith MP-30	University of New Mexico Electrical Engineering Albuquerque, NM 87131 Attn: H. Southward	RCA Sarnoff Research Center P.O. Box 432 Princeton, NJ 08540 Attn: K. Zaininger
Martin Marietta Corp P.O. Box 179 Denver, CO 80201 Attn: B.T. Graham MS PO-454	Northrop Corp Electronic Division 1 Research Park Palos Verdes Penin, CA 90274 Attn: B.T. Ahlport	Rensselaer Polytechnic Inst P.O. Box 965 Troy, NY 12181 Attn: R.J. Gutmann
Martin Marietta Corp P.O. Box 179 Denver, CO 80201 Attn: J.R. McKee Bus Lib 6617	Northrop Corp Electronic Division 1 Research Park Palos Verdes Penin, CA 90274 Attn: G.H. Towner	Research Triangle Institute P.O. Box 12194 Research Triangle Park, NC27709 Attn: Sec Officer for M. Simons

Rockwell International P.O. Box 3105 Anaheim, CA 92803 Attn: J.E. Bell HA10	Science Applications, Inc 8400 Westpark Drive McLean, VA 22101 Attn: W.L. Chadsey	TRW Defense & Space Sys Group One Space Park Redondo Beach, CA 90278 Attn: Tech Info Ctr S-1930
Rockwell International P.O. Box 3105 Anaheim, CA 92803 Attn: G.C. Messenger FB61	Simulation Physics, Inc P.O. Box D Bedford, MA 01730 Attn: R.G. Little	TRW Defense & Space Sys Group One Space Park Redondo Beach, CA 90278 Attn: R.M. Webb RI-2410
Rockwell International P.O. Box 3105 Anaheim, CA 92803 Attn: D.J. Stevens FA70	Singer Company 150 Totowa Road Wayne, NJ 07470 Attn: Tech Info Center	TRW Defense & Space Sys Group One Space Park Redondo Beach, CA 90278 Attn: R.K. Plebuch RI-2078 (2)
Rockwell International P.O. Box 3105 Anaheim, CA 92803 Attn: K.F. Hull	Singer Company 1150 McBride Ave Little Falls, NJ 07424 Attn: I. Goldman	TRW Defense & Space Sys Group One Space Park Redondo Beach, CA 90278 Attn: H.H. Holloway RI-2036
Rockwell International P.O. Box 3105 Anaheim, CA 92803 Attn: N.J. Rudie FA53	Sperry Rand Corp Marcus Avenue Great Neck, NY 11020 Attn: C.L. Craig	TRW Defense & Space Sys Group P.O. Box 1310 San Bernardino, CA 92402 Attn: R. Kitter
Rockwell International Collins Division 400 Collins Road NE Cedar Rapids, IA 52406 Attn: D. Sutherland	Sperry Rand Corp Marcus Avenue Great Neck, NY 11020 Attn: P. Maraffino	TRW Defense & Space Sys Group P.O. Box 1310 San Bernardino, CA 92402 Attn: F.B. Fay
Sanders Associates, Inc 95 Canal Street Nashua, NH 03060 Attn: M.L. Aitel NCA 1-3236	Stanford Research Institute 333 Ravenswood Ave Menlo Park, CA 94025 Attn: P.J. Dolan	TRW Defense & Space Sys Group P.O. Box 1310 San Bernardino, CA 92402 Attn: E.W. Allen 520/141
Science Applications, Inc P.O. Box 2351 La Jolla, CA 92038 Attn: L. Scott	Stanford Research Institute 306 Wynn Drive, NW Huntsville, AL 35805 Attn: M. Morgan	Vought Corp P.O. Box 5907 Dallas, TX 75222 Attn: Tech Data Center
Science Applications, Inc P.O. Box 2351 La Jolla, CA 92038 Attn: J.R. Beyster	Sundstrand Corp 4751 Harrison Ave Rockford, IL 61101 Attn: C.B. White	Westinghouse Electric P.O. Box 1693 Baltimore-Washington Internat'l Baltimore, MD 21203 Attn: H.P. Kalapaca MS 3525
Science Applications, Inc 2109 W. Clinton Ave Suite 700 Huntsville, AL 35805 Attn: N.R. Byrn	Texas Instruments, Inc P.O. Box 5747 Dallas, TX 75222 Attn: D.J. Manus MS 72	Jet Propulsion Laboratory California Institute of Tech 4800 Oak Grove Drive Pasadena, CA 91103 Attn: J. Maserjian MS 198-229
Science Applications, Inc 2680 Hanover Street Palo Alto, CA 94303 Attn: C. Stevens	TRW Defense & Space Sys Group One Space Park Redondo Beach, CA 90278 Attn: O.E. Adams RI-1144	(2)